

Straintronics and twistronics in bilayer graphene

Federico Escudero,^{1,*} Dong Wang,^{2,*} Pierre A. Pantaleón,¹
Shengjun Yuan,^{2,3,4} Francisco Guinea,^{1,5} and Zhen Zhan^{1,†}

¹IMDEA Nanoscience, Faraday 9, 28049 Madrid, Spain

²Key Laboratory of Artificial Micro- and Nano-structures of Ministry of Education
and School of Physics and Technology, Wuhan University, Wuhan 430072, China

³School of Artificial Intelligence, Wuhan University, Wuhan 430072, China

⁴Wuhan Institute of Quantum Technology, Wuhan, 430206, China

⁵Donostia International Physics Center, Paseo Manuel de Lardizábal 4, San Sebastián 20018, Spain

(Dated: February 4, 2026)

The interplay of twist and strain in bilayer graphene enables the formation of moiré patterns and narrow bands that host correlated and topological phases. While magic-angle twisted bilayer graphene has been widely studied, strain provides an additional and realistic control knob for band engineering. In this work, we first generate a global method to construct commensurate supercells for arbitrary twist and strain. Then, using atomistic tight-binding and strain-extended continuum models to study the commensurate structures, we identify configurations that minimize the bandwidth beyond the magic angle. The results reveal a strong dependence of band narrowing and topology on strain type, magnitude, direction and lattice relaxation. Particularly, shear strain produces a stronger distortion than uniaxial strain. Including electron-electron interactions through a self-consistent Hartree potential shows that strain broadens the bare bands while reducing electrostatic renormalization. Strain also drives topological transitions as the narrow and remote bands hybridize, establishing twisted and strained bilayer graphene as a tunable platform for flat-band and topological phenomena.

I. INTRODUCTION

The discovery of correlated phases and unconventional superconductivity in twisted bilayer graphene (TBG) has attracted significant attention over the last few years [1–11]. These phenomena are intrinsically connected to the emergence of very flat bands due to the moiré potential [12–15], induced by the lattice mismatch created by the twist or strain [16–21]. The quenching of the kinetic energy in the flat bands promotes the appearance of the observed electronic correlations. Any approach to understand the nature of the correlated phases in TBG must then start from a solid understanding of the nature and origin of the flat bands, supported by accurate modelling methods.

With only a relative twist, the flat bands are well-known to arise at an infinite set of *magic angles*, the largest one being around 1° [12, 15, 22]. However, in practice the samples usually have at least some residual strain [23, 24], defects [25–27] or even twist angle disorders [28–30], typically arising during their fabrication [31]. The presence of strains, in particular, can significantly modify the geometrical and electronic properties of the system since the moiré acts as a magnifying glass [20, 21, 32–37]. Although this may be seen as undesirable, one can conversely use strains as an additional tune parameter in the system [23, 33, 38–40]. Compared to the twist, which only rotates the layers, strains distort the layers and thus can lead to a plethora

of moiré patterns with potentially rich properties [21, 41]. This has motivated recent experimental advances in developing new techniques to induce and manipulate the strain in moiré heterostructures [40, 42–44], opening a path to straintronics and twistronics, whereby the electronic properties can be tuned by the combined interplay between twist and strain. Among different types of strain, uniaxial heterostrain is the most common type, and has been observed in many experimental samples [4, 32, 34, 37, 45]. Consequently, most theoretical works focus on the effects of the uniaxial heterostrain. Recently, under some new well-developed techniques, shear heterostrain is introduced to manipulate the moiré patterns [46–48].

A natural question, then, is how does the presence of arbitrary strain and twist modifies the narrow bands in twisted bilayer graphene. An initial step involves computing the electronic spectra of the system and study its evolution under different kinds of relevant strain. Since narrow bands generally arise only under small lattice mismatches [12, 15], at which the supercells can contain tens of thousands of atoms, previous studies have mostly employed extensions of effective continuum models under strain [19–21], or topological heavy fermion models [49, 50]. Yet, despite its importance, there is no comprehensive study of the electronic properties under strain by means of more realistic approaches, such as atomistic models. The challenge for that relies not only on the huge size of the supercell, but also on the fact that under twist and strain the system is in general incommensurate, and it is not clear at which configurations there can actually be a commensurate solution [51]. The commensurate and incommensurate structures may in fact have

* These authors contributed equally to this paper.

† zhenzhanh@gmail.com

distinct ground-state properties [52].

In this work, we present a comprehensive analysis of the tight-binding (TB) properties of twisted and strained bilayer graphene (TSBG), focusing on the optimal conditions for the emergence of narrow bands. Two relevant types of strain are considered: uniaxial and shear. We first tackle the problem of obtaining commensurate structures under both twist and strain. We find that by generally adding a small biaxial strain, one can always find particular twist and strain values at which the system is commensurate. Using these commensurate structures, we then obtain the band structure and the density of states (DOS) by using a full atomistic TB model. We find that: (i) albeit the strain tends to increase the bandwidth at the (nonstrain) magic angle [20, 21], there are yet other twist angles at which the bandwidth can be minimum, resulting in a shift of magic angle with strain; (ii) the emergence of narrow bands depends critically on the strain direction; (iii) the shear strain produces a stronger distortion of the geometry and electronic properties of TSBG; (iv) the gap between the narrow and remote bands (induced by the lattice relaxation) is mainly determined by the strain-dependent bandwidth of the narrow bands.

Our atomistic results are then compared with that of the strain-extended continuum model [53–56], which introduces two main modifications: (i) the change in the moiré vectors by which electrons in the different layers are coupled through the moiré potential [21, 41]; (ii) the introduction of strain-induced fields [57, 58]. We show that with just a few suitable parameter choices, the continuum model yields results in excellent agreement with the TB ones. In particular, we find that the strain-induced gauge potential, accounting for the change in the hopping energies within the Dirac approximation [57], plays a key role in capturing the electronic behavior in TSBG. Using the strain-extended continuum model, we extend our analysis of the bandwidth evolution under twist and strain. We find that the twist angle at which the bandwidth is minimum sensitively depends on the strain direction. Yet, we remarkably see that the minimum bandwidth of the narrow bands (at the optimal twist angle) increases practically linearly with the strain magnitude.

We further consider the effect of electrostatic interactions, as accounted by the Hartree potential [59–61]. Due to the increase of bandwidth under strain, the Hartree effect is weaker than that in the only twisted configurations. Consequently, as the strain increases, there is a competition between the increase of bandwidth of the bare bands, and the decrease of the Hartree potential. We show the synergy between these effects can lead to bandwidths under twist and strain that are actually comparable, if not smaller, than those with only twist angles. As any comprehensive account of correlated phases must consider such strong renormalization of the spectra by electrostatic interactions [62–66], we conclude that TSBG has the potential to be a platform for new and rich correlated phenomena.

Finally, we analyze the influence of strain on the topology of the narrow bands around the magic angle. By introducing a small mass term that breaks the inversion symmetry, we compute the valley Chern number C of the narrow bands for different strain magnitudes and directions. Due to the strain effect in both increasing the narrow bandwidth and reducing the remote bandgap, there are topological ($C = \pm 1$) to trivial ($C = 0$) transitions as the strain increases, with a non-trivial dependence on the strain direction. We show that these topological transitions take place when the narrow bands close their gap with the remote bands. In the noninteracting case, we find that the sum of Chern number in top and bottom narrow band is always zero, i.e., they are both topological or both trivial. However, upon taking into account the electrostatic interactions we find asymmetrical topological transitions, whereby one narrow band can be topological while the other is trivial. We associate this behavior to the asymmetrical renormalization of the narrow bands due to the Hartree potential, which implies that they close their gap with the remote bands at different strain magnitudes.

The paper is organized as follow: In Sec. II, we introduce a general formalism for moiré commensurability with any twist and strain, and discuss the Dirac point shifts due to the moiré deformation. In Sec. III, we calculate the electronic structures by using the TB and continuum methods, including the uniaxial strain, shear strain and lattice relaxations. These two models yield results in excellent agreement. Then, we investigate the narrow band modulation by both twist and strain. In Sec. IV, we study the effect of the electronic interactions. The band topology with strain is investigated in Sec. V. Our conclusions follow in Sec. VI.

II. MOIRÉ COMMENSURABILITY WITH TWIST AND STRAIN

In order to employ the TB method to obtain the band structure, we first require a commensurate structure. Although for only twist configurations the set of commensurate twist angles is well known, there is no close expression for the set of twist and strain that give commensurate structures. In what follows we will explicitly describe a global method to construct a commensurate structure of TSBG for a given twist angle and strain, taking into account different types of strain observed in experiments.

A. Structural analysis of the moiré patterns

1. Commensurate structures with twist

We consider two graphene layers rotated in the plane by an angle θ , with the rotation origin at the AA site, and assume the constructed supercell is commensurate with

only one moiré pattern [67]. Each moiré pattern contains three different high-symmetry stackings, namely AA, AB and domain wall (DW) stackings, similar to the strained configuration shown in Fig. 1(a). For the non-strain case, the rotation angle for the commensurate condition is [12, 68]

$$\cos \theta = \frac{3i^2 + 3i + 1/2}{3i^2 + 3i + 1}, \quad i = 0, 1, 2, \dots \quad (1)$$

where i is an integer. The commensurate supercell vectors are

$$\begin{aligned} \mathbf{L}_1 &= i\mathbf{a}_1 + (i+1)\mathbf{a}_2, \\ \mathbf{L}_2 &= -(i+1)\mathbf{a}_1 + (2i+1)\mathbf{a}_2, \end{aligned} \quad (2)$$

where $\mathbf{a}_1 = a(1, 0)$ and $\mathbf{a}_2 = a(1/2, \sqrt{3}/2)$ are the lattice vectors of monolayer graphene, with $a \simeq 2.46\text{\AA}$ being the lattice constant. Therefore, a commensurate supercell with twist angle θ and vectors $\mathbf{L}_{1,2}$ is exclusively identified by the integer i .

When strain is introduced into the system, Eqs. (1) and (2) become invalid, and a general formalism is needed to determine the twist, strain and moiré vectors of the commensurate structure.

2. Uniaxial, shear and biaxial strains

We introduce three important strains that are reported by experiments. An arbitrary two-dimensional strain tensor is given by

$$\mathcal{E} = \begin{pmatrix} \epsilon_{xx} & \epsilon_{xy} \\ \epsilon_{xy} & \epsilon_{yy} \end{pmatrix}, \quad (3)$$

where $\epsilon_{ij} = (\partial u_i / \partial x_j + \partial u_j / \partial x_i) / 2$, with \mathbf{u} the displacement vector that accounts for the deformation induced by stress [69, 70]. The three relevant types of strain that we shall consider are uniaxial, shear and biaxial (Figs. 1(c)-(e)). Their corresponding strain tensors read [20, 21, 41, 53]

$$\mathcal{E}_u = R_\phi \begin{pmatrix} \epsilon & 0 \\ 0 & -\nu\epsilon \end{pmatrix} R_{-\phi} \quad (\text{uniaxial}), \quad (4)$$

$$\mathcal{E}_s = R_\phi \begin{pmatrix} 0 & \epsilon \\ \epsilon & 0 \end{pmatrix} R_{-\phi} \quad (\text{shear}), \quad (5)$$

$$\mathcal{E}_b = \begin{pmatrix} \epsilon & 0 \\ 0 & \epsilon \end{pmatrix} \quad (\text{biaxial}). \quad (6)$$

Here $R_\phi \equiv R(\phi)$ is the rotation matrix, ϵ is the strain magnitude, ϕ is the strain direction relative to the x axis, and ν is the Poisson's ratio ($\nu \simeq 0.16$ in graphene). The shear strain can be written as

$$\mathcal{E}_s = R_{\phi+\pi/4} \begin{pmatrix} \epsilon & 0 \\ 0 & -\epsilon \end{pmatrix} R_{-\phi-\pi/4}. \quad (7)$$

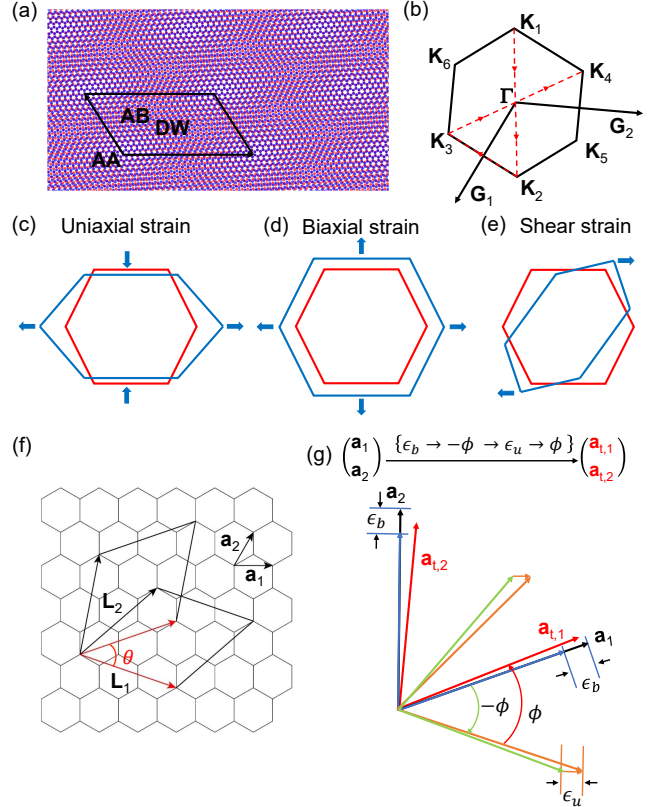


FIG. 1. (a) Moiré pattern of bilayer graphene with a twist angle $\theta = 3.89^\circ$ and uniaxial strain $\epsilon_u = 3.7\%$. The atoms in the top and bottom layers are plotted with blue and red dots, respectively. The AA, AB and DW stacking regions are labeled. Due to the strain the AA regions are elliptical. (b) Illustration of the moiré Brillouin zone, with the reciprocal lattice vectors labeled by \mathbf{G}_1 and \mathbf{G}_2 . We label six corner K points. The red dashed line is the momentum path for the band structure plots. (c), (d), (e) Schematically show the uniaxial, biaxial and shear strains, respectively. Only the top layer (blue line) is deformed. The undeformed bottom layer is plot with red lines. (f) Schematic construction of the moiré cell with the lattice vectors of the two graphene layers. (g) Schematic construction of the moiré cell in three steps by following the Eq. (9) with $\mathcal{E} \rightarrow \mathcal{E}_b + \mathcal{E}_{u/s}$: (1) an isotropic rescaling corresponding to ϵ_b ; (2) an anisotropic rescaling corresponding to ϵ_u in a direction given by ϕ ; (3) a rotation by an angle θ . We only plot the first two steps in (g).

Comparing with the uniaxial strain tensor we then have the relation

$$\mathcal{E}_s(\epsilon, \phi) = \mathcal{E}_u(\epsilon, \phi + \pi/4, \nu \rightarrow 1). \quad (8)$$

This means that a shear strain with magnitude ϵ and direction ϕ_s can be thought as uniaxial strain with magnitude ϵ and direction $\phi_u = \phi_s + \pi/4$, but with Poisson's ratio $\nu \rightarrow 1$ (i.e., the limit case in which the lateral contraction is equal to the applied longitudinal tension).

In this paper, we restrict ourselves to TBG with a heterostrain, which refers to relative strains between two layers. Specifically, we assume that the top layer is strained

and the bottom layer is rotated. Note that our definition of heterostrain differs from that in Refs. [20, 21], where the two layers are strained in opposite directions with equal magnitude, i.e. a symmetric configuration. Instead, our definition is closer to the experimental cases in Ref. [4, 32], where the concept of heterostrain was first introduced. These two types of heterostrain show slightly different modification of the geometrical and electronic properties of the moiré systems. However, these two definitions induce practically the same perturbation effects to the TBG around the first magic angle and are indistinguishable in both theory [71] and experiment [46].

3. Moiré geometry with twist and strain

An application of strain in the top layer, and a rotation in the bottom layer, transform their lattice vectors as

$$\begin{aligned}\mathbf{a}_{t,i} &= (\mathbb{I} + \mathcal{E}) \mathbf{a}_i, \\ \mathbf{a}_{b,i} &= R_\theta \mathbf{a}_i,\end{aligned}\quad (9)$$

where \mathbb{I} is the 2×2 identity matrix. The reciprocal vectors follow as

$$\begin{aligned}\mathbf{b}_{t,i} &= (\mathbb{I} + \mathcal{E})^{-1} \mathbf{b}_i, \\ \mathbf{b}_{b,i} &= R_\theta \mathbf{b}_i,\end{aligned}\quad (10)$$

where \mathbf{b}_i are the reciprocal lattice vectors of the honeycomb lattice. The reciprocal moiré vectors \mathbf{G}_i (see Fig. 1(b)) can then be calculated by taking the difference between the deformed lattice vectors in each layer [18, 21, 41, 72]

$$\mathbf{G}_i = \mathbf{b}_{t,i} - \mathbf{b}_{b,i}. \quad (11)$$

The real space moiré vectors \mathbf{L}_i are determined by the relation $\mathbf{L}_i \cdot \mathbf{G}_j = 2\pi\delta_{ij}$. In principle, the moiré vectors \mathbf{G}_i and \mathbf{L}_i define the moiré structure [20, 41]. However, in practice, the definition of \mathbf{L}_i does not guarantee commensurability in the supercell.

4. Commensurate structures with twist and strain

In this part, we develop a general geometrical formalism for commensurate structures in TSBG. The analysis of the commensurate supercell can be performed by expressing the moiré lattice vectors as function of those of the two graphene layers, as shown in Fig. 1(f)

$$\begin{pmatrix} \mathbf{L}_1 \\ \mathbf{L}_2 \end{pmatrix} = \begin{pmatrix} i & j \\ k & l \end{pmatrix} \begin{pmatrix} \mathbf{a}_{t,1} \\ \mathbf{a}_{t,2} \end{pmatrix} = \begin{pmatrix} m & n \\ q & r \end{pmatrix} \begin{pmatrix} \mathbf{a}_{b,1} \\ \mathbf{a}_{b,2} \end{pmatrix}. \quad (12)$$

Then the top and bottom graphene lattice can be related by a Park-Madden transformation matrix

$$\begin{aligned}\begin{pmatrix} \mathbf{a}_{t,1} \\ \mathbf{a}_{t,2} \end{pmatrix} &= \frac{1}{il - jk} \begin{pmatrix} lm - jq & ln - jr \\ -km + iq & -kn + ir \end{pmatrix} \begin{pmatrix} \mathbf{a}_{b,1} \\ \mathbf{a}_{b,2} \end{pmatrix} \\ &= \begin{pmatrix} a & b \\ c & d \end{pmatrix} \begin{pmatrix} \mathbf{a}_{b,1} \\ \mathbf{a}_{b,2} \end{pmatrix}.\end{aligned}\quad (13)$$

For an arbitrary transformation matrix composed of contributions of twist and strain, there are four variables (a, b, c, d) corresponding to a pair of eight integers (i, j, k, l, m, n, q, r) that define the Park-Madden matrix. The set of eight integers can be determined experimentally through atomically-resolved microscopy [32, 72].

The analysis of the commensurate supercell also can be expressed as a function of the elementary geometrical deformations in Eq. (9), which in general depends on four parameters: the twist angle and the three components of the strain tensor. These four parameters completely determine, in principle, the (2×2) matrix in Eq. (13). If, for simplicity, one assumes that the system contains only uniaxial or shear strain, then one is left with only three parameters, namely, the twist and the strain magnitude and direction. Therefore, we introduce an additional - extremely small - biaxial strain in the top layer, so that Eq. (9) becomes $\mathbf{a}_{t,i} \rightarrow (\mathbb{I} + \mathcal{E}_{u/s} + \mathcal{E}_b) \mathbf{a}_i$ [see Fig. 1(g)]. Then the system has four parameters $(\theta, \epsilon_{u/s}, \phi, \epsilon_b)$ that can *fully* determine the set of eight integers in Eq. (13). To obtain the commensurate solutions, it is convenient to rewrite $\mathbf{a}_{t,i} \simeq (\mathbb{I} + \mathcal{E}_b) (\mathbb{I} + \mathcal{E}_{u/s}) \mathbf{a}_i$ by taking $\mathcal{E}_b \mathcal{E}_{u/s} \rightarrow 0$ under the limit of small deformations. The transformation matrix that links $(\mathbf{a}_{t,1}, \mathbf{a}_{t,2})$ with $(\mathbf{a}_{b,1}, \mathbf{a}_{b,2})$ can then be written as

$$\begin{pmatrix} \mathbf{a}_{t,1} \\ \mathbf{a}_{t,2} \end{pmatrix} = P (1 + \epsilon_b) (\mathbb{I} + \mathcal{E}_{u/s}) R_\theta P^{-1} \begin{pmatrix} \mathbf{a}_{b,1} \\ \mathbf{a}_{b,2} \end{pmatrix}, \quad (14)$$

where $P = \begin{pmatrix} 1 & 0 \\ 1/2 & \sqrt{3}/2 \end{pmatrix}$ is the basis of the triangular lattice vectors. By combining then Eqs. (13) and (14) we can relate the physical parameters $(\theta, \epsilon_{u/s}, \phi, \epsilon_b)$ to the eight integers (i, j, k, l, m, n, q, r) [72].

The described procedure to obtain commensurate structures can be generalized to any arbitrary strain tensor, with the inclusion of lattice relaxation effects [73]. A detailed, step-by-step algorithm of how to obtain commensurate structures with any twist and strain, with some example solutions, can be found in the Secs. S1 and S2.

B. Dirac point shifts from moiré geometry deformation

When the strain is small, we can consider that the length of the two moiré vectors remains, to a first approximation, practically equal. In that case, the borders of the mBZ are given by the three points (see Fig. 1(b)) [21]:

$$\begin{aligned}\mathbf{K}_1 &= -\frac{(1 + 2\chi)\mathbf{G}_1 - \lambda\mathbf{G}_2}{2(1 + \chi)}, \\ \mathbf{K}_3 &= \mathbf{K}_1 + \mathbf{G}_1, \\ \mathbf{K}_5 &= \mathbf{K}_1 + \mathbf{G}_1 - \lambda\mathbf{G}_2,\end{aligned}\quad (15)$$

and their negatives. Here $\chi = |\mathbf{G}_1 \cdot \mathbf{G}_2|/|\mathbf{G}_1 \cdot \mathbf{G}_1|$ and $\lambda = \text{sign}(\mathbf{G}_1 \cdot \mathbf{G}_2) + \delta_{0, \mathbf{G}_1 \cdot \mathbf{G}_2}$. When the angle between

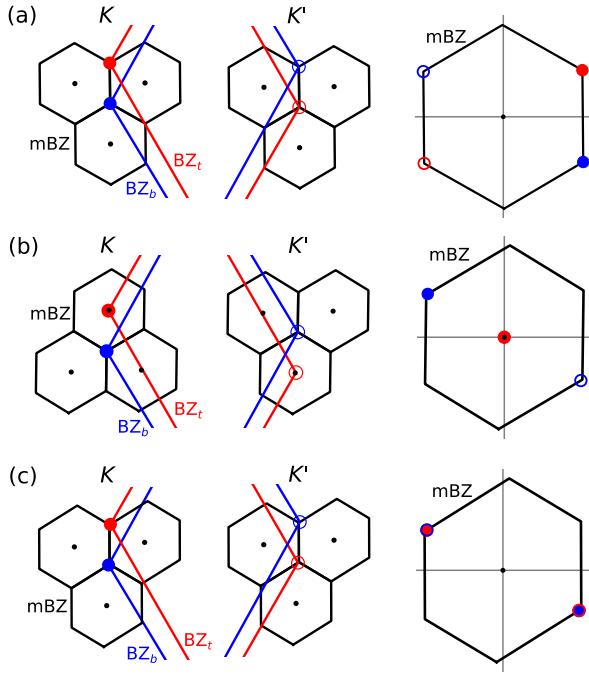


FIG. 2. (a) Position of the Dirac points projected within the mBZ, for the commensurate solutions of magic angle $\theta \sim 1.05^\circ$ without strain. (b) The same case as (a) for uniaxial strain $\epsilon_u \sim 0.1\%$. (c) The same case as (a) for shear strain $\epsilon_s \sim 0.1\%$. In each case, plots on the left and middle sides show the Dirac points in the top (red) and bottom (blue) layers, and the mBZ periodically translated from the origin for the K and K' valleys, respectively. Plots on the right side show the position of the Dirac points within the mBZ, when translated by the moiré vectors. In (b) and (c), the positions of Dirac points from the top strained layer are slightly shifted from the five possible positions in the mBZ.

\mathbf{G}_1 and \mathbf{G}_2 is 120° , the moiré pattern is triangular and the points above collapse to yield a hexagonal mBZ.

Next, we check how the undeformed Dirac points, at the corners of the graphene BZ, are mapped into the mBZ. First we translate Eq. (12) to the reciprocal space as:

$$\begin{pmatrix} \mathbf{b}_{t,1} \\ \mathbf{b}_{t,2} \end{pmatrix} = \begin{pmatrix} i & j \\ k & l \end{pmatrix} \begin{pmatrix} \mathbf{G}_1 \\ \mathbf{G}_2 \end{pmatrix},$$

$$\begin{pmatrix} \mathbf{b}_{b,1} \\ \mathbf{b}_{b,2} \end{pmatrix} = \begin{pmatrix} m & n \\ q & r \end{pmatrix} \begin{pmatrix} \mathbf{G}_1 \\ \mathbf{G}_2 \end{pmatrix}. \quad (16)$$

The projection of a Dirac point at $\mathbf{K}_0 = \mathbf{b}_1/3 + 2\mathbf{b}_2/3$ is then given by:

$$\begin{aligned} \mathbf{K}_0 &= (\mathbf{G}_1 \ \mathbf{G}_2) \begin{pmatrix} \frac{1}{3}i + \frac{2}{3}j \\ \frac{1}{3}k + \frac{2}{3}l \end{pmatrix} \\ &= (\mathbf{G}_1 \ \mathbf{G}_2) \begin{pmatrix} \frac{1}{3}m + \frac{2}{3}n \\ \frac{1}{3}q + \frac{2}{3}r \end{pmatrix}. \end{aligned} \quad (17)$$

For different pairs of (i, j, k, l, m, n, q, r) , there are five different types of projections: $(0, 0)$, $(0, \frac{1}{3})$, $(\frac{1}{3}, 0)$, $(\frac{1}{3}, \frac{1}{3})$,

$(\frac{1}{3}, \frac{2}{3})$. These projections will always fall into the five high-symmetry points.

The situation under strain changes because the borders of the mBZ are no longer located at $\mathbf{G}_1/3 + 2\mathbf{G}_2/3$ (and translations by reciprocal moiré vectors), as in the non-strain case. Consequently, the Dirac points in the mBZ are rather located at arbitrary, strain-dependent positions. Some examples of the geometrical positions of the Dirac points in TSBG are plotted in Figs. 2(b)-(c). The Dirac points are effectively away from the corners of the mBZ, and are no longer degenerate. It should be noted that our analysis here only accounts for the geometrical position of the Dirac points in each layer, i.e., the projection of the borders of their respective BZ. As we will discuss in the following sections, under strain and relaxation the Dirac points are also slightly shifted by strain-induced fields. Moreover, due to the broken symmetries under strain, the actual position of the moiré Dirac points is further influenced by the moiré potential that couples the two layers [21, 36, 71].

In the particular non-strain case, the commensurate condition is given by Eq. (1), and Eq. (17) becomes

$$\mathbf{K}_0 = (\mathbf{G}_1 \ \mathbf{G}_2) \begin{pmatrix} 2/3 \\ 1/3 \end{pmatrix}, \quad (18)$$

which means that if there is no strain, the Dirac cones are always projected to the corners of the mBZ (Fig. 2(a)). As discussed in the following section, the shift of the Dirac cones and the deformation of the mBZ under strain explain why, in the TB calculations, the K_1 , K_2 , K_3 , K_4 and Γ points appear displaced compared to the unstrained case.

C. Numerical models

We first compute the electronic structure of commensurate TSBG by using a full atomistic TB Hamiltonian. Then, we construct a general effective continuum model to describe the TB results. A key step for comparing the TB and continuum results is identifying the Dirac points in the strained mBZ, discussed in Sec. II B (see also Fig. 2).

1. Tight-binding model

The TB Hamiltonian of the TSBG is generated by only considering the p_z orbital of the carbon atom as [68]

$$H = \sum_i \varepsilon_i c_i^\dagger c_i + \sum_{\langle i,j \rangle} t_{ij} c_i^\dagger c_j \quad (19)$$

where c_i is an annihilation operator for the i state, ε_i is the on-site potential, $\langle i, j \rangle$ is the sum over index with $i \neq j$, t_{ij} is the hopping integral between i and j orbitals, which follows the Slater-Koster (SK) formalism. As detailed above, including a very small biaxial strain

guarantees commensurate solutions for arbitrary twist and uniaxial/shear strain, from which we calculate the bands. For conciseness, in the main text we quote the approximate twist and strain values of the commensurate solutions. The exact strain and twist parameters are listed in Sec. S2. We identify the valley character with a valley operator [74, 75], and relax the moiré supercell with LAMMPS [76]. Details of the TB calculations are given in Sec. S3.

2. Strain-extended continuous model

In the continuum model, the electronic properties of the system are accounted by the coupling of the Dirac points in each layer with an effective moiré-induced interlayer potential. Neglecting couplings between different valleys in each layer, the continuum model Hamiltonian for the K valley takes the form [20, 32, 77]

$$H = \begin{pmatrix} h_b(\mathbf{k}) + \mathcal{S}_b & U^\dagger(\mathbf{r}) \\ U(\mathbf{r}) & h_t(\mathbf{k}) + \mathcal{S}_t \end{pmatrix}, \quad (20)$$

where the index $\ell = b, t$ refers to the bottom and top layers, respectively. $h_\ell(\mathbf{k})$ is the Dirac Hamiltonian relative to the twisted and strained Dirac points:

$$h_\ell(\mathbf{k}) = -\hbar v \boldsymbol{\sigma} \cdot R_{\theta_\ell} (1 + \mathcal{E}_\ell) (\mathbf{k} - \mathbf{K}_\ell), \quad (21)$$

where $\boldsymbol{\sigma} = (\sigma_x, \sigma_y)$ are the Dirac matrices and $\mathbf{K}_\ell = (1 - \mathcal{E}_\ell) R_\ell(\theta_\ell) \mathbf{K}_0$, where $\mathbf{K}_0 = -(2\mathbf{b}_1 + \mathbf{b}_2)/3$ is the Dirac point of a honeycomb layer. The strain introduces an additional term \mathcal{S}_ℓ that includes a deformation and gauge potential [54, 57, 58, 78, 79]

$$\mathcal{S}_\ell = \mathbb{I}V_\ell - \hbar v \boldsymbol{\sigma} \cdot R_{\theta_\ell} (1 + \mathcal{E}_\ell) \mathbf{A}_\ell, \quad (22)$$

where

$$V_\ell = g(\epsilon_{xx}^\ell + \epsilon_{yy}^\ell), \quad (23)$$

$$\mathbf{A}_\ell = \frac{\sqrt{3}}{2a} \beta (\epsilon_{xx}^\ell - \epsilon_{yy}^\ell, -2\epsilon_{xy}^\ell), \quad (24)$$

with $g = 4$ eV and $\beta = 3.14$ for graphene [20, 54]. The scalar potential V_ℓ shifts the Dirac points in energy, resembling the effect of a perpendicular electric field. The vector potential \mathbf{A}_ℓ shifts the Dirac points in momentum and accounts for the strain-induced change in the hopping energies within the Dirac approximation [57, 58].

The moiré-induced coupling potential $U(\mathbf{r})$ depends on the interplay between twist and strain through its Fourier expansion in terms of the moiré vectors [17, 18, 21]. At small deformations (i.e., low twist and strain) the Fourier expansion can be truncated to the first three leading order terms [21]:

$$U(\mathbf{r}) = U_1 + U_2 e^{i\mathbf{G}_1 \cdot \mathbf{r}} + U_3 e^{i(\mathbf{G}_1 + \mathbf{G}_2) \cdot \mathbf{r}}, \quad (25)$$

where

$$U_j = \begin{pmatrix} u_0 & u_1 e^{-\omega_j} \\ u_1 e^{\omega_j} & u_0 \end{pmatrix}, \quad (26)$$

with $\omega_j = (j - 1) 2\pi/3$. Here u_0 and u_1 are the effective AA and AB/BA hopping amplitudes. The values of these hopping energies are expected to depend on the local lattice deformations. In general, a rigid configuration implies equal hopping energies $u_0 = u_1$. This results in the remote bands always touching the flat middle bands, i.e., there is no gap between them [15, 17]. However, relaxation effects tend to shrink and increase the interlayer distance of the energetic AA regions, compared to the most favorable AB/BA, thus leading to an effective smaller hopping $u_0 < u_1$ [80–82]. The main effect of this is to open a gap between the flat middle bands and the remote bands. For the numerical calculations we set the values of u_0 and u_1 , as well as the Fermi velocity v , to the best fit with the TB results.

III. ELECTRONIC STRUCTURES

A. Strain effect

Figure 3 shows both the TB and continuum model results for the band structure and DOS at the first magic angle $\theta \sim 1.05^\circ$, for different cases: without strain, and with uniaxial and shear strains, both with directions $\phi = 0$ (see also Figs. S1 - S4 for the cases with $\theta = 1.6^\circ$ and $\theta = 0.93^\circ$, and different strain strength). The TB intralayer and interlayer hopping parameters are $t_0 = 2.8$ eV and $t_1 = 0.44$ eV, respectively. The fitted continuum model parameters $u_0 = u_1 = 0.1$ eV and $\hbar v/a = 2.15$ eV provide excellent agreement with the TB calculations. As described below, strain introduces four generic features in the electronic structures.

First, the middle narrow bands are extremely sensitive to strain. In the absence of strain, the band structure at the first magic angle exhibits characteristic flat bands near the charge neutrality point (CNP), leading to a pronounced peak in the DOS. Upon introducing strain into the system, we see that the narrow peak splits into two peaks in the DOS, with reduced magnitude [83]. The strain broadens the width (the difference between the extreme values within one band) of the narrow bands. Moreover, the energy separation (indicated by the separation of the van Hove singularities (vHs)) between the conduction (CB) and valence (VB) bands increases with increasing strain strength (see Figs. 3, S1, S13). In TSBG with $\theta = 1.6^\circ$, strain induces multiple DOS peaks from both the valence and conduction bands, showing that strain can effectively generate higher-order vHs [20, 32, 34]. We emphasize that for each twist angle, the minimum bandwidth always appears around the small strain region (see narrow band dome in Fig. S5).

Second, the strain breaks the C_3 symmetry and lifts the valley degeneracy along the high-symmetry points of the mBZ [20, 32, 84]. In the unstrained case, the Dirac points are located at the corners of the mBZ. The conduction and valence narrow bands are connected by two Dirac crossings in each valley, protected by the $C_{2z}T$ symmetry.

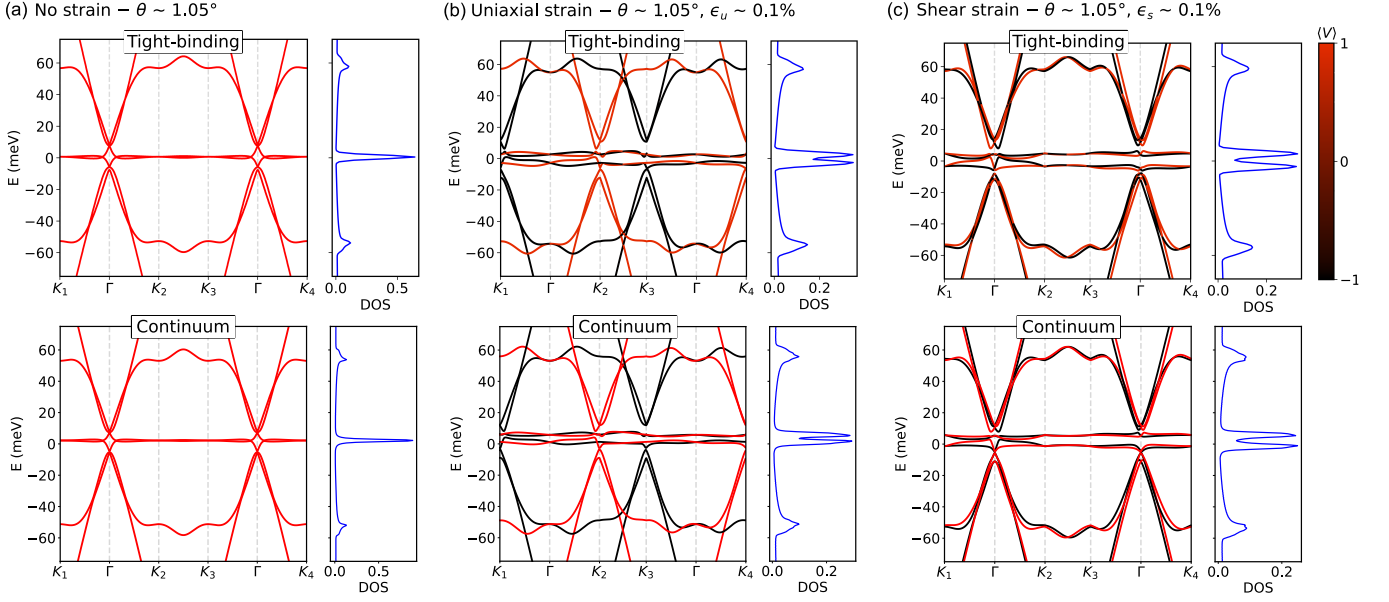


FIG. 3. Band structure and DOS for the commensurate structures of TBG with $\theta = 1.05^\circ$, $\phi = 0^\circ$ and (a) no strain, (b) uniaxial strain $\epsilon_u = 0.1\%$, (c) shear strain $\epsilon_s = 0.1\%$, calculated by the TB (top panel) and continuum (bottom panel) models. In the TB band structures of (b) and (c), the color represents the expectation of the valley operator, with $\langle \hat{V}_z \rangle \approx 1$ if a state belongs to valley K (red line) and $\langle \hat{V}_z \rangle \approx -1$ if a state belongs to valley K' (black line). The momentum path is illustrated in Fig. 1(b).

When strain is introduced, the breaking of C_3 symmetry lifts the valley degeneracy, as confirmed by the expectation value of the valley operator at each band state (details in Sec. S3). In the band structure, this manifests as a separation between the red and black curves corresponding to different valleys. A similar valley splitting occurs in TBG/hBN heterostructures, where the aligned hBN substrate breaks valley degeneracy [84, 85]. This lifting of valley degeneracy may account for the experimentally observed fourfold, rather than eightfold, Landau level degeneracy near the CNP [3, 5]. Nevertheless, the band structures of the K and K' valleys remain related by time-reversal symmetry, and the conduction and valence narrow bands stay connected, indicating that strain alone cannot open a gap in TBG due to the preserved $C_{2z}T$ symmetry.

Third, the Dirac points are no longer located at the corner of the mBZ, but rather around the five possible positions. This further reflects the lack of C_3 symmetries in the presence of strain. The geometric position of the Dirac points with 0.1% strain (uniaxial and shear) are plotted in Figs. 2(b)-(c). However, the exact positions of the Dirac points, identified from the energy maps (Fig. 6), are found to be slightly different. As noted before, and discussed in detail in the continuum model results, there are two additional sources of corrections of the Dirac point position: (i) the gauge potential induced by strain (external strain and lattice relaxation); (ii) the deformed moiré potential that couples the two graphene layers. Moreover, there is an energy shifting of the two Dirac points within a valley, resulting in a finite (lower)

density of states at the CNP.

Finally, we observe that the remote bands always give two additional peaks flanking the middle narrow bands, which do not change under low strain. In particular, the DOS peaks around ± 60 meV from the remote bands are unchanged in the presence of strain (see also Fig. S13). This behavior is consistent with recent experimental results that suggest that the remote bands are insensitive to strain [46] and their optical interband transitions can be used as a fingerprint of the twist angle [86].

B. Comparison between uniaxial and shear strain

When comparing the effects of uniaxial and shear strain, we observe clear differences. Under shear strain, the energy separation between the vHs is larger, and the middle bands become narrower across most regions of the mBZ (see also Fig. 6). This can be attributed to geometric modulation: for the same strain magnitude, shear strain produces a stronger distortion of the moiré pattern than uniaxial strain, see Eq. (8) and also Fig. S8. Similar trends are found for twist angles beyond the first magic angle (see Figs. S3 and S4).

Within the continuum model, the difference between the uniaxial and shear strain effect can be related to their corresponding scalar and gauge potentials. For uniaxial strain, the scalar potential is independent of the strain direction

$$V_u = g\epsilon(1-\nu) \sim 3.35\epsilon \text{ eV}, \quad (27)$$

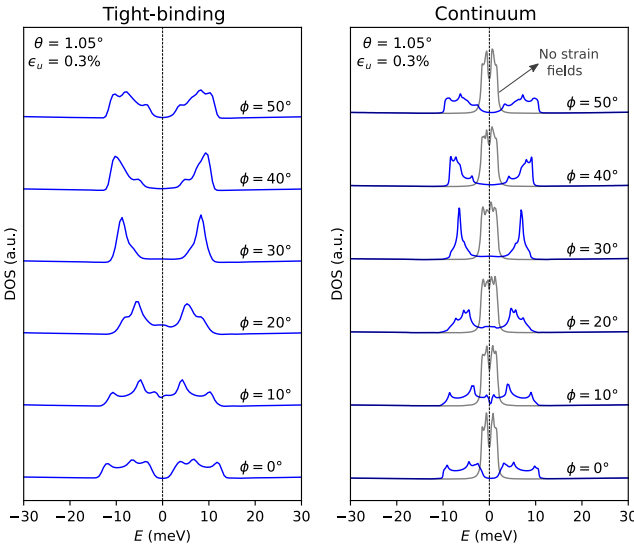


FIG. 4. Evolution of DOS with uniaxial strain direction ϕ in TSBG with $\theta = 1.05^\circ$ and $\epsilon_u = 0.3\%$, calculated by the TB (left side) and continuum (right side) models. We label $E = 0$ meV with black vertical dashed lines. The curves are relatively shifted to make the plot clear.

while for shear strain it vanishes, $V_s = 0$. On the other hand, the magnitude of the vector potential for uniaxial reads

$$|\mathbf{A}_u| = \frac{\sqrt{3}}{2a} \beta \epsilon (1 + \nu) \sim 12.8 \epsilon \text{ nm}^{-1}, \quad (28)$$

which is independent of the strain direction. For shear strain one has the same expression, but with $\nu \rightarrow 1$ [or, equivalently, with a strain magnitude $\epsilon_s \rightarrow \epsilon(1 + \nu)$]; see Eq. (8). Since $|\mathbf{K}| \sim 17 \text{ nm}^{-1}$ in graphene, the momentum space shift induced by \mathbf{A} is very small at low strain magnitudes, even on the scale of the moiré BZ. However, such a small shift can still significantly alter the electronic properties. It is worth noting that the net shift of the decoupled Dirac points in each monolayer, namely $\mathbf{K} \rightarrow (1 - \mathcal{E}) R_\theta \mathbf{K}^0 - \mathbf{A}$, does not generally match the actual position of the moiré Dirac points within the mBZ. This is due to the effect of the moiré potential and the role of the strain in breaking the symmetries of the system [21].

C. Strain direction effect

In unstrained TBG, the system possesses sixfold rotational symmetry, allowing the strain direction to be restricted to the range $\phi \in [0, 60^\circ]$. Since uniaxial and shear strains are related by a 45° rotation [cf. Eq. (8)], we focus on the uniaxial case. The evolution of the DOS as a function of strain direction is shown in Fig. 4 (see also Figs. S6, S7, S12). The results agree well with previous continuum model studies [20]. We again observe an excellent agreement between the TB and continuum results.

Interestingly, we see that the main features of the DOS, namely the highly sensitive splitting of the vHs as a function of the strain direction, is well captured only when the strain fields V and \mathbf{A} are included. Thus, although the strain effect in the continuum model Hamiltonian generally comes from both the change in the moiré potential $U(\mathbf{r})$ (due to the geometric variation of the strained moiré vectors) and the inclusion of the strain-induced potential \mathcal{S}_ℓ , the latter seem to have a greater effect on the middle narrow bands.

As the strain direction changes, the DOS peaks exhibit strong variations in both intensity and energy, particularly for $\theta = 1.05^\circ$. At the magic angle, when $\phi = 30^\circ$ only one prominent peak appears in each band, while for $\theta = 1.6^\circ$ a sharp peak emerges at the CNP when $\phi = 20^\circ$ (Fig. S7). The strain direction also shifts the position of the Dirac points within the mBZ (see Fig. S6). Our results reveal an important aspect often overlooked in previous studies: the strain direction plays a decisive role in determining both the bandwidth and the energy separation of the narrow bands.

Specifically, we observe that at low twist angles the main effect of the strain on the electronic properties - in particular the strain direction - comes from the gauge potential \mathbf{A} . For any rotation ϕ of the strain tensor $\mathcal{E} \rightarrow R_\phi \mathcal{E} R_{-\phi}$, as considered in Fig. 4, the gauge potential \mathbf{A} transforms as

$$\mathbf{A}(\mathcal{E}) \rightarrow \mathbf{A}(R_\phi \mathcal{E} R_{-\phi}) = R_{-2\phi} \mathbf{A}(\mathcal{E}), \quad (29)$$

that is, it simply rotates by -2ϕ . Thus, the magnitude of the gauge potential is invariant, and only the direction of \mathbf{A} changes when the strain direction is modified. The high sensitivity of the DOS to the strain direction around the magic angle, as seen in Fig. 4, then reflects that it is the actual direction of the vector potential that plays the most significant role in modifying the electronic spectra. This is in line with previous studies indicating that the moiré coupling, and the emergence of flat bands, depends critically on the relative orientation between the Dirac points and the momentum transfer vectors [20, 21, 87].

In fact, in linear Dirac band systems, the gauge potential is the relevant term that significantly modifies the electronic properties [20]; the scale potential only shifts the Dirac points in energy, which is safely ignored in the continuum model [20, 21]. However, in parabolic band systems, the scale potential has a prominent contribution to the band structure, for example, controlling the energy gap and flattening the band edges [88]. In particular, in the rhombohedral multilayer graphene with a quasi-one dimensional geometry, the scalar term¹ induces enriched correlated behaviors.

¹ The relevant effect of the scalar potential is brought to our attention by discussions with Haim Beidenkopf's group.

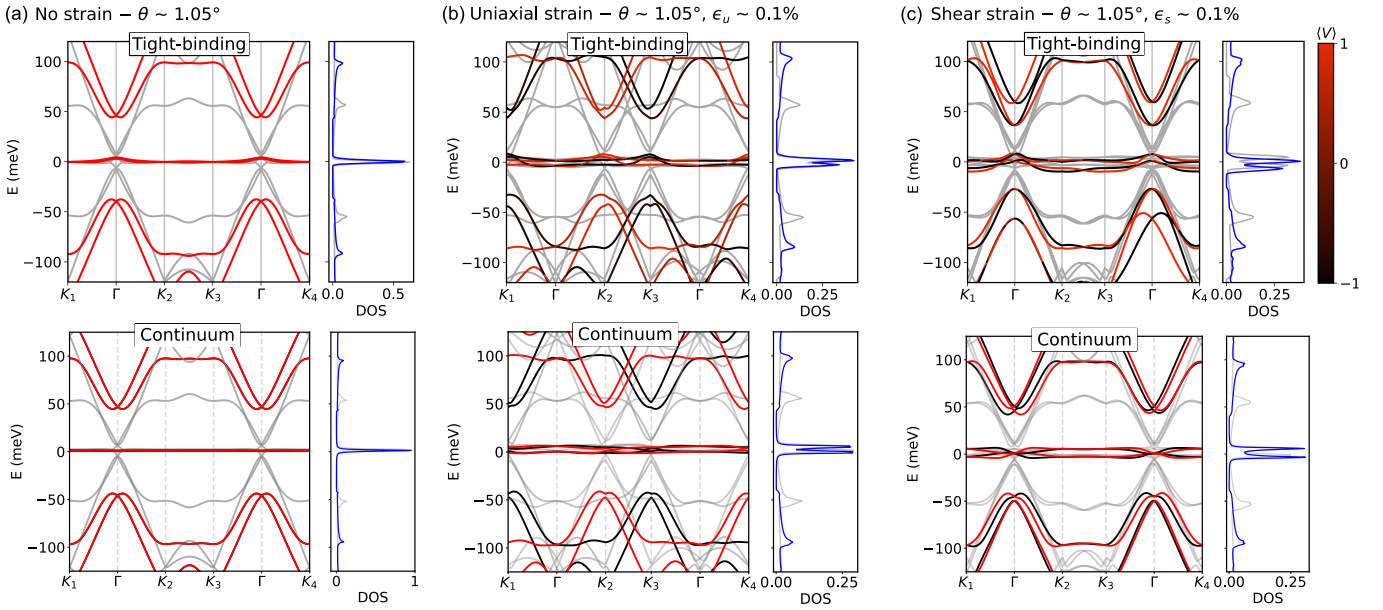


FIG. 5. Band structure and DOS for relaxed TBG with $\theta = 1.05^\circ$ and (a) no strain, (b) uniaxial strain $\epsilon_u = 0.1\%$, (c) shear strain $\epsilon_s = 0.1\%$. The band structure and DOS of rigid cases are plotted with gray dots. The colors in the band structure are the same as in Figure 3. Note that, in the plots, the energy range in the relaxed case is almost two times larger than the energy range of the rigid case.

D. Lattice relaxation effect

The relaxed geometry exhibits two main global features (see Sec. S7). First, the lattice relaxation patterns of graphene moiré structures, with and without strain, are qualitatively similar: the AA regions shrink, while the AB regions expand into triangular domains [89]. Second, strain drives a structural transition in the DW network [47]. In nonstrain TBG, the DWs are of the shear type, characterized by a Burgers vector parallel to the DW. When strain is applied, the angle between the Burgers vector and the DW boundary changes, leading to a mixed configuration containing both shear and tensile DWs [90, 91]. The atomic displacements within the DW region differ significantly between the strained and unstrained cases. This structural discrepancy may alter the electronic states localized at the DWs, which typically lie at higher energies [92, 93]. Note that the local AA, AB and DW regions are distorted, which require additional corrections when we consider the lattice relaxation effect in the continuum model that demands for future study [94].

Figure 5 presents a comparative analysis of the relaxed and rigid band structures and DOS under strain in both TB and continuum cases. The simplest way to account for relaxation effects in the continuum model is to consider an unequal ratio $u_0 < u_1$ between the hopping energies of AA and Bernal stacking. To fit the TB results we consider $u_1 = 0.096$ eV, $u_0 = 0.05952$ eV and $\hbar v/a = 2.13$ eV. The obtained results show again good agreement with the TB results with relaxation.

The most notable effect remains the gap opening between the remote and narrow bands induced by relaxation. Moreover, the lattice relaxation increases the energy separation between the valence and conduction narrow bands, and broadens the width of the narrow bands, as also shown in Fig. 6. Interestingly, lattice relaxation introduces a pronounced electron–hole asymmetry in the TB results. The DOS peak in the conduction band is larger than that in the valence band, although both peaks exhibit nearly equal magnitudes at $\theta = 0.93^\circ$ and $\theta = 1.6^\circ$ (see Fig. S10). The asymmetry between the DOS peaks associated with the narrow bands, as well as its evolution with twist angle, is consistent with recent experimental observations in which similar behavior was reported as the twist angle and strain were varied in the same device [46]. Note that the continuum model does not capture the small particle-hole asymmetry around the flat bands, which is mainly due to the stronger relaxation in the valence bands. To capture such behavior one generally has to introduce additional non-local contributions in the moiré potential, which here we neglect [95]. Moreover, we find that the gap between the remote conduction and valence bands remains nearly constant under strain, while the separation between the remote and narrow bands decreases as strain increases, reflecting their broadening.

E. Narrow bands with strain and twist

In line with the TB results, the continuum model reflects that the strain effectively increases the bandwidth

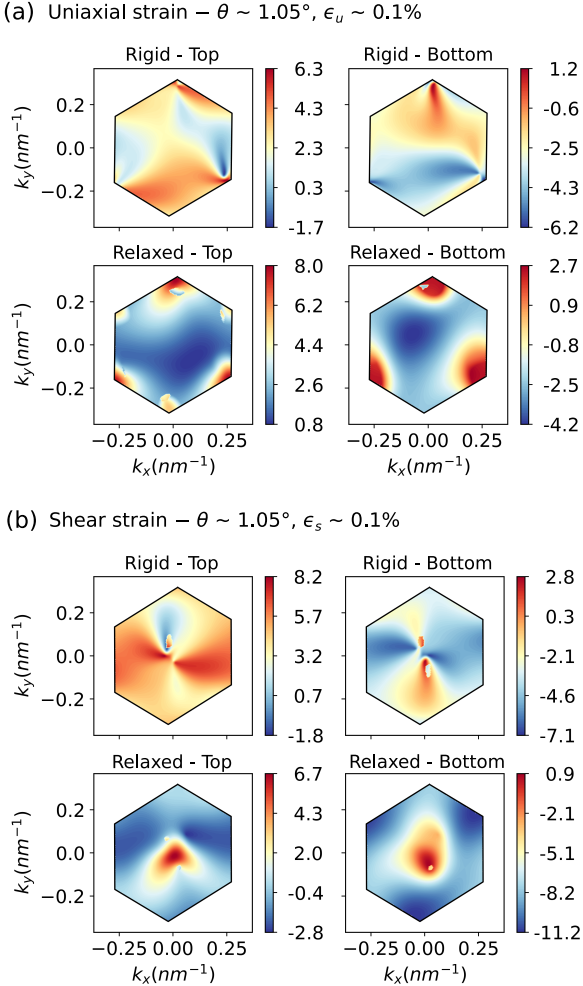


FIG. 6. Comparison of energy map of the top and bottom narrow bands (tight-binding results) between relaxed and rigid TBG with $\theta = 1.05^\circ$ and (a) uniaxial strain $\epsilon_u = 0.1\%$, (b) shear strain $\epsilon_s = 0.1\%$. The mBZ is illustrated with black line. The color represents the energy with unit meV. We only show the energy map of narrow bands from valley K in the mBZ, which are identified by the valley operator.

of the narrow bands around the magic angle. Nevertheless, there is always a minimum bandwidth depending on the twist and strain. Thus, one can still identify potential twist and strain configurations at which electronic correlations could be maximized. Here, we shall particularly focus on the identification of the twist angle at which the bandwidth of the narrow bands is minimum.

Figure 7 shows the bandwidth evolution as a function of the twist angle θ and the uniaxial strain magnitude ϵ , with different directions ϕ , for the relaxed configuration of continuum model parameters. In general, we observe that the twist angle at which the bandwidth is minimum tends to shift in the presence of strain. The shift is nonuniform and depends non-trivially on the strain direction. Thus, we observe that as the strain magnitude increases, the magic angle tends to increase when $\phi = 0^\circ$,

but it tends to decrease when $\phi = 30^\circ$. For shear strain one obtains a similar behavior as in Fig. 7, only that the effect is stronger for the same strain magnitude, and the dependence with the strain direction is shifted [cf. Eq. (8)].

Remarkably, the minimum bandwidth always seems to follow a linear dependence with the strain magnitude [20]. We have checked that this behavior persists even without the strain-fields (see Fig. S14). The main difference then is that the bandwidth evolution becomes almost insensitive to the strain direction, but scales linearly with the strain magnitude. Such linear dependence of the bandwidth is roughly due to the linear dependence of the moiré vector with the strain strength [see Eq. (11)], which introduce the strain effect through the moiré potential given by Eq. (25).

It should be noted that under strain a minimum bandwidth does not necessarily correlate to a higher DOS. This is because with strain the narrow bands are not, in general, uniformly flat over the whole mBZ. A band at a particular twist and strain configuration can have, for instance, a larger bandwidth than at other configuration, but yet be flatter over a wider region of the mBZ. Consequently, the configuration with higher bandwidth would still have higher vHs. In this sense, a minimum bandwidth should only be considered as an indicator for the appearance of strong electronic correlations.

Although a nonzero strain tends to increase the bandwidth, it is crucial such an increase depends on the twist angle. Since most samples are, at least, likely to inherit some kind of random strain [4, 10, 96, 97] (e.g., due to their fabrication method), which can vary from sample to sample, our results highlight that the notion of *magic angle* is intrinsically connected to the experimental conditions of the system.

IV. STRAIN AND ELECTROSTATIC INTERACTIONS

Our analysis so far has neglected the role of electron-electron interactions in the system. However, these interactions are actually crucial in the narrow band regime due to the quenching of the kinetic energy. In this section we will address, in particular, the role of the electrostatic interactions within the continuum model, as accounted by the Hartree potential [59–61]. Our main interest will be the effect of electrostatic interactions on the bandwidth and charge density of the twisted and strained bilayer configurations.

The Hartree interaction is the direct (classical) interaction of an electron with the surrounding charge density:

$$V_H(\mathbf{r}) = \int d\mathbf{r}' v_C(\mathbf{r} - \mathbf{r}') \delta\rho(\mathbf{r}'), \quad (30)$$

where $v_C(\mathbf{r} - \mathbf{r}')$ is the bare Coulomb potential and $\delta\rho(\mathbf{r}')$ is the electronic charge density with respect to

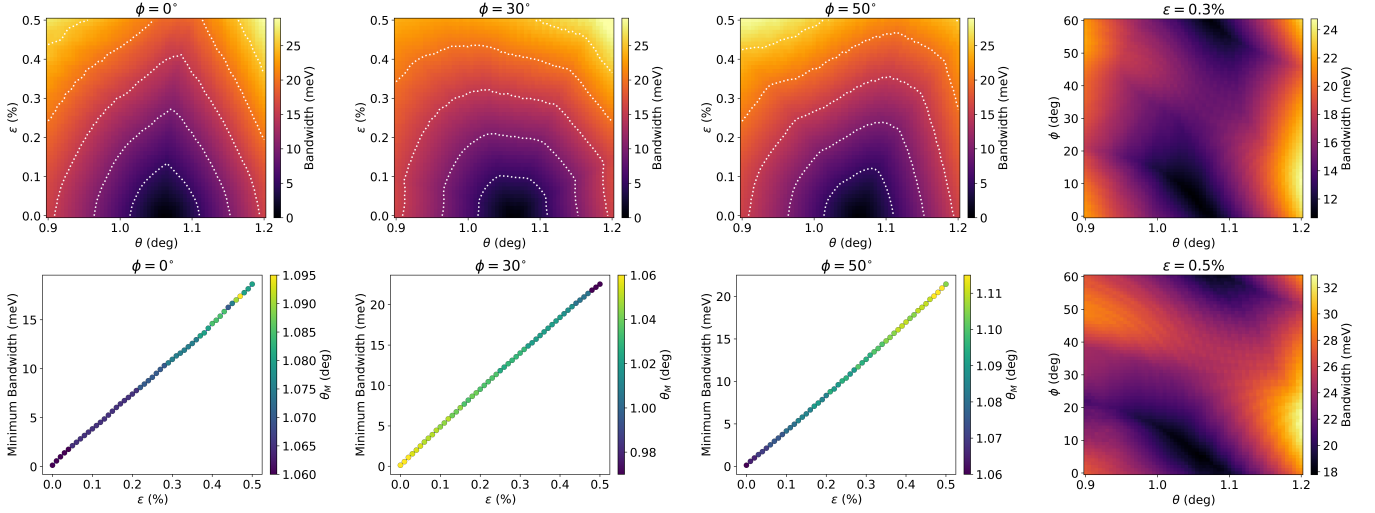


FIG. 7. Numerical continuum model results for the bandwidth evolution in the top narrow band, as a function of the twist angle θ and: (i) uniaxial strain magnitude ϵ along fixed directions $\phi = 0^\circ, 30^\circ, 50^\circ, 60^\circ$; white dotted-lines indicate constant bandwidths from 5 to 25 meV, in steps of 5 meV. (ii) strain direction for fixed magnitudes $\epsilon = 0.3\%, 0.5\%$. The first three bottom panels show the minimum bandwidth at θ_M (right colorbar) as a function of the strain magnitude ϵ , following an almost linear relation. All the results correspond to the *relax* configuration with parameters $\hbar v/a = 2.13$ eV, $u_1 = 0.096$ eV and $u_0 = 0.05952$ eV.

CNP. Replacing the plane-wave expansion of the Bloch states in TSBG leads to

$$V_H(\mathbf{r}) = \sum_{\mathbf{G} \neq 0} V_H(\mathbf{G}) e^{-i\mathbf{G} \cdot \mathbf{r}}, \quad (31)$$

$$V_H(\mathbf{G}) = \frac{v_C(\mathbf{G})}{A_c} \sum_{\mathbf{k}, \mathbf{G}'} \sum'_{n, \eta, i} u_{n, \mathbf{k}, \eta, i}^*(\mathbf{G}' + \mathbf{G}) u_{n, \mathbf{k}, \eta, i}(\mathbf{G}'), \quad (32)$$

where $u_{n, \mathbf{k}, \eta, i}(\mathbf{G})$ are the Fourier coefficients of the band, valley/spin and layer/sublattice indices n, η, i , respectively, and $v_C(\mathbf{G})$ is the Fourier transform of the bare Coulomb potential (see Sec. S12 for details). We consider a gated configuration of two metallic plates [98], for which $v_C(\mathbf{G}) = e^2 \tanh(d|\mathbf{G}|)/2\epsilon_0\epsilon_r|\mathbf{G}|$, where d is the distance between the two metallic plates, and ϵ_r is the relative primitivity of the system. For the numerical calculations we set $d = 40$ nm. Note that the $\mathbf{G} = 0$ term in $V_H(\mathbf{r})$ is neglected because it is canceled by the background positive charge (jellium model) [59, 99].

In unstrained TBG, the moiré pattern is perfectly triangular, and the largest Fourier components of the Hartree potential correspond to the first six reciprocal vectors of equal magnitude [59, 60]. Owing to the C_3 symmetry, each reciprocal vector contributes equally to the charge density and the Hartree potential, which therefore follow the same spatial profile [60]. Under strain, however, the moiré pattern becomes distorted and loses its triangular symmetry [21, 41], making the contributions from different Fourier components inequivalent. As a result, the Hartree potential is no longer proportional to the charge density. In our numerical calculations, we therefore include all Fourier components $V_H(\mathbf{G})$ within the reciprocal moiré vectors of the continuum model.

The Hartree potential is diagonal in the valley/spin and sublattice/layer flavors, with matrix elements [100]

$$\langle \mathbf{k} + \mathbf{G}' - \mathbf{G}, \eta', i' | \hat{V}_H | \mathbf{k} + \mathbf{G}', \eta, i \rangle = \delta_{\eta\eta'} \delta_{ii'} V_H(\mathbf{G}). \quad (33)$$

Since the Hartree potential depends on the occupied Bloch states from CNP, the total Hamiltonian $\hat{H} = \hat{H}_0 + \hat{V}_H$ is solved self-consistently, for different filling factors, up until convergence.

Figure 8 shows the numerical results for the evolution of the band structure and density of states, from CNP ($\nu = 0$), to a filling of $\nu = +2$ (two electrons per moiré unit cell), for different dielectric constants ϵ_r . The results correspond to $\theta = 1.05^\circ$ with no strain (top panels), and uniaxial strain with magnitude $\epsilon = 0.1\%$ and direction $\phi = 30^\circ$ (bottom panels). In both cases, we observe that as the dielectric constant diminish and the Hartree potential increases, the band structure is strongly reshaped [59–61, 101].

Interestingly, by comparing the nonstrain with the strain case, we observe that the interacting band structures end up having similar bandwidths, despite having quite different single-particle bandwidth. This is because the Hartree potential diminish as the bare active bands increase their bandwidth, essentially due to the decrease in the quenching of the kinetic energy. As a result, under strain there is a competition between the increase of the non-interacting bandwidth and the decrease of the Hartree potential. The synergy between both effects determines the effective bandwidth under strain and electrostatic interactions. It may actually be that under strain the net bandwidth becomes comparable, or even smaller, than the one corresponding to the no-strain scenarios.

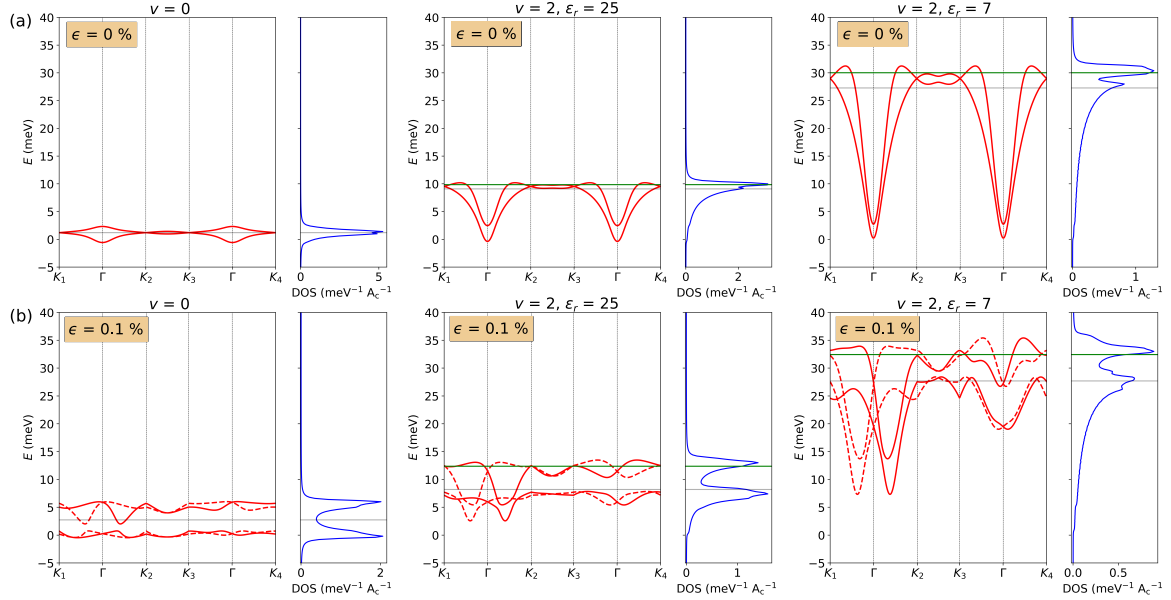


FIG. 8. Evolution of the band structure and DOS as a function of the electrostatic interactions (self-consistent Hartree), from the non-interacting case at charge neutrality (filling $\nu = 0$), to a filling $\nu = 2$ with different dielectric constants ϵ_r . Panel (a) shows the results for the no strain case at $\theta = 1.05^\circ$, while panel (b) shows the results for $\theta = 1.05^\circ$ and uniaxial strain with magnitude $\epsilon = 0.1\%$ and direction $\phi = 30^\circ$. In all cases, the horizontal gray and green lines indicate the CNP and the Fermi level, respectively. In the band structures, the solid and dashed lines correspond to the K and K' valleys. All the results are for the relaxed configuration with continuum model parameters $\hbar v/a = 2.13$ eV, $u_1 = 0.096$ eV and $u_0 = 0.0592$ eV.

As the strain increases, the Hartree effect not only weakens but also evolves into a nearly uniform energy shift. In other words, it changes from a non-rigid shift in the unstrained case, to an almost rigid (and small) shift at larger strains. This behavior indicates that the charge density across different momentum points becomes increasingly uniform as strain grows. Figure 9 illustrates this transition from non-rigid to rigid behavior, for the case of uniaxial strain. While the non-interacting and interacting bands differ noticeably at low strain, they become nearly identical at higher strain values, implying that the Hartree potential becomes effectively negligible. The strain threshold for this transition depends non-trivially on the strain direction (and, more generally, on the strain type). It also varies with the filling factor because of the asymmetric Hartree renormalization of the conduction and valence bands, depending on whether the system is electron- or hole-doped.

V. BAND TOPOLOGY WITH STRAIN

The strain-induced reshaping of the electronic properties in TSBG is expected to influence the valley-dependent topology of the band structure. Previous studies have indeed reported a rich topological phase diagram arising from the interplay between twist and strain, both in TMDs [20] and in bilayer graphene [77, 102]. However, a detailed analysis of how the topology of the narrow bands in TSBG evolves with different types of

strain is still lacking.

Since strain preserves time-reversal symmetry, the Chern numbers of opposite valleys remain equal in magnitude and opposite in sign, yielding an overall zero Chern number, i.e., a topologically trivial system. Nevertheless, each valley can still host non-trivial topology. A clear signature of such valley topology, even without breaking time-reversal symmetry, is the nonlinear Hall effect [103, 104], which can be used to probe the topological character of the narrow bands [105]. In what follows, we therefore focus on the valley-resolved topology of the TSBG band structure.

We study the topology evolution of the bands by computing the Chern number

$$\mathcal{C}_n = \frac{1}{2\pi} \int \boldsymbol{\Omega}_n(\mathbf{k}) \cdot d\mathbf{k}, \quad (34)$$

where $\boldsymbol{\Omega}_n(\mathbf{k}) = i \langle \partial_{\mathbf{k}} \psi_{n\mathbf{k}} | \times | \partial_{\mathbf{k}} \psi_{n\mathbf{k}} \rangle$ is the Berry curvature of the n -band Bloch states $\psi_{n\mathbf{k}}$, $d\mathbf{k}$ is a reciprocal-space surface vector, and the integration is over a moiré unit cell. To obtain \mathcal{C}_n numerically we use the Fukui-Hatsugai-Suzuki method [106], considering different strain parameters. For comparison, we analyze separately both the noninteracting and the interacting cases with electrostatic interactions. All the results are obtained using the continuum model for the relaxed configuration. The Chern numbers are computed for the top and bottom narrow bands by introducing a small mass term $\sim m\sigma_z$ in the TSBG Hamiltonian that breaks the inversion symmetry and opens a gap at the Dirac points.

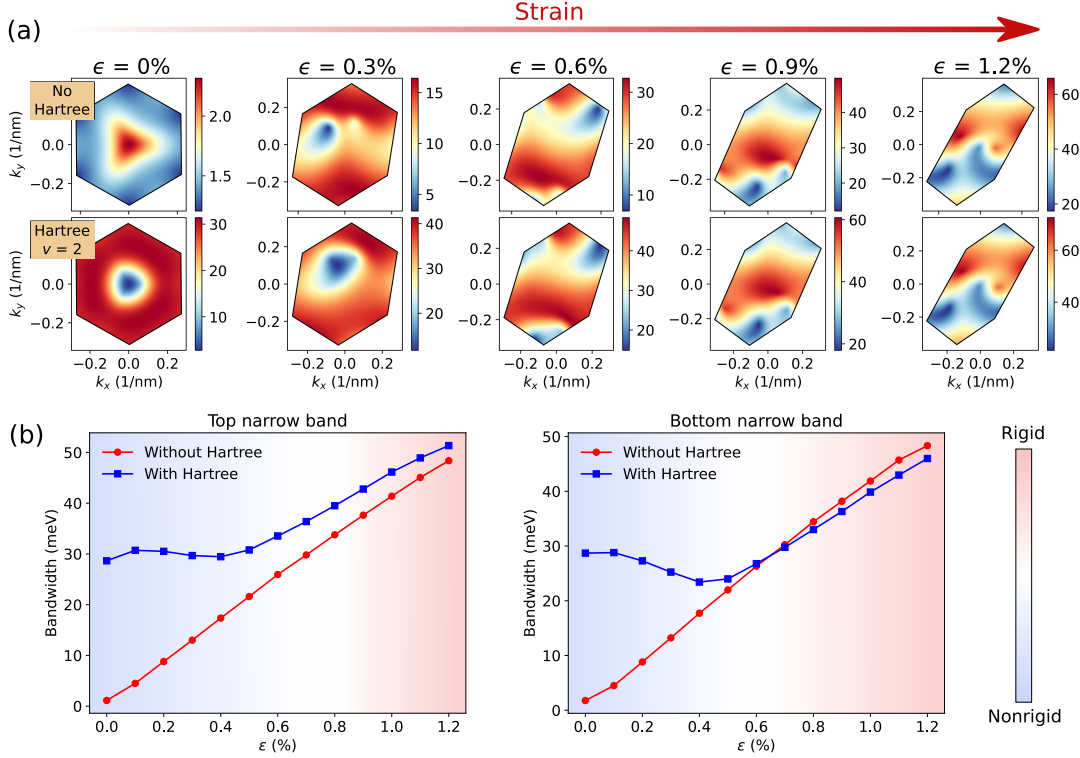


FIG. 9. Evolution from a nonrigid to a rigid Hartree effect as the strain increases. Panel (a) shows the continuum model density plot of the top narrow band for $\theta = 1.05^\circ$ and uniaxial strain with direction $\phi = 20^\circ$ and increasing strain magnitudes ϵ . The top and bottom density panels show, for each strain magnitude, the bands without Hartree and with Hartree (filling $\nu = 2$ and $\epsilon_r = 7$), respectively. Panel (b) shows the bandwidth in the top and bottom narrow bands, with and without Hartree, as a function of the uniaxial strain magnitude ϵ with direction $\phi = 20^\circ$; other parameters as in panel (a). The colormap indicates, schematically, the nonrigid to rigid transition as the strain increases and the bandwidths become similar.

A. Non-interacting case

Figure 10 shows the results for the non-interacting case at $\theta = 1.05^\circ$ under uniaxial and shear strain with different directions ϕ and magnitudes ϵ . When interaction effects are neglected, the two narrow bands retain opposite Chern numbers of equal magnitude, so their total Chern number remains zero. In the absence of strain, the upper and lower narrow bands are topological with valley Chern numbers of +1 and -1, respectively. Upon introducing strain, a topological transition to trivial narrow bands ($C = 0$) occurs when the gap between the narrow and remote bands closes and reopens. This behavior arises because the strain increases the bandwidth of the narrow bands and simultaneously shifts the remote bands to lower energies (see Fig. 5). The critical point at which the gap closes depends nontrivially on the strain magnitude and direction, and, in general, also on the twist angle. Interestingly, the non-interacting band topology is preserved up to relatively large strain magnitudes ($\epsilon \sim 2\%$).

The strain-induced touching between the narrow and the remote bands that triggers the topological transition is accompanied by a transfer of charge density. Figure 12 shows this transfer of charge density $\rho_{\mathbf{k}}(\mathbf{r})$ for uniaxial

strain (non-interacting case), at the momentum point \mathbf{k} of minimum (direct) gap between the narrow and remote bands. As clearly seen, the charge density of the topological band ($C = 1$) is directly transferred to the remote band after the gap closes and the narrow band becomes trivial ($C = 0$). This charge transfer behavior occurs, in general, for any kind of twist and strain that induce a remote gap closing. The dependence on the specific type of strain is reflected in the profile of the charge density transferred (e.g., its symmetries), and the specific twist and strain parameters at which the topological transition takes place. For biaxial strain, for instance, the system retains the C_3 symmetry and the topological transition involves the transfer of ring-like to AA centered charge densities between the top and remote bands (Sec. S13).

B. Interacting case

Figure 11 shows the topology evolution of the narrow bands after including electrostatic interactions. In contrast to the noninteracting case, we now see that by increasing the strain magnitude the topology of the top and bottom narrow bands becomes asymmetrical. That is, there are now strain configurations for which the sum

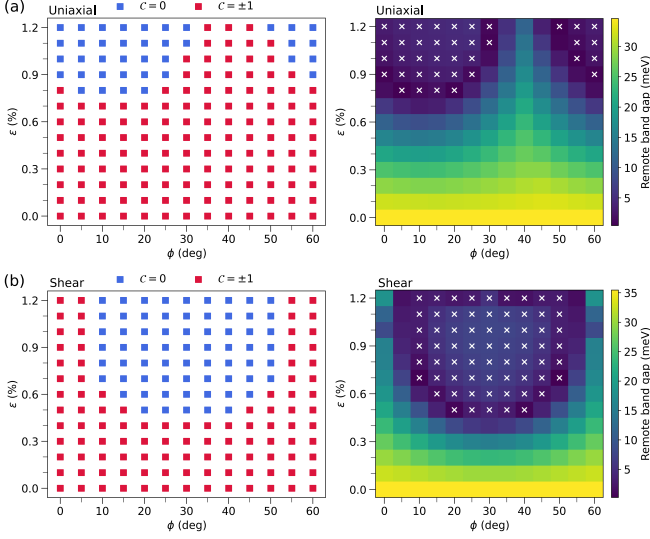


FIG. 10. Strain-induced topology evolution of the narrow bands, for the non-interacting case at $\theta = 1.05^\circ$ with (a) uniaxial heterostrain and (b) shear strain. In each case, the top left panel show the Chern number in the top and bottom narrow bands as a function of the strain direction ϕ and magnitude ϵ . For all parameters, $C = +1 (-1)$ for the top (bottom) bands. The top right panel shows the gap between the top narrow bands and the remote bands. The minimum gap, at which it closes and then re-opens, corresponds to the topological transitions $|C| = 1 \rightarrow 0$ in (a); the white crosses indicate the regions where the narrow bands are trivial ($C = 0$).

of the top and bottom band Chern number is not zero. This is because for any nonzero filling the Hartree potential reshapes the top and bottom bands asymmetrically, cf. Fig. 8. In general, for positive fillings ν (electron-doped) the bottom narrow band is more strongly renormalized, and vice versa for negative fillings ν . This leads to different strain parameters at which the gap with the remote bands closes and then re-opens, and therefore, wider strain regimes in which only one band is topological. Compared to the noninteracting case of Fig. 10, we particularly see that the Hartree potential shrinks and increase, respectively, the regimes where the bottom and top bands are topological. Since the Hartree potential is practically symmetric with respect to charge neutrality [59, 60], the regime in which only one band is topological is reversed when the system is hole-doped ($\nu < 0$).

It is interesting to compare the strain with other perturbations in their capacity to modify the topology of the narrow bands. Table I list the topology effect of four common perturbations in TBG: Strain, Hartree (electrostatic interactions), substrate and displacement field. For a fixed twist angle (e.g., the magic angle), only a strain [77, 102] or a substrate [100] can, by itself, modify the topology of the central narrow bands. In contrast, the topology of the narrow bands cannot be changed by means of solely electrostatic interactions [59, 60] or a displacement field [107, 108]. Note that when two or more

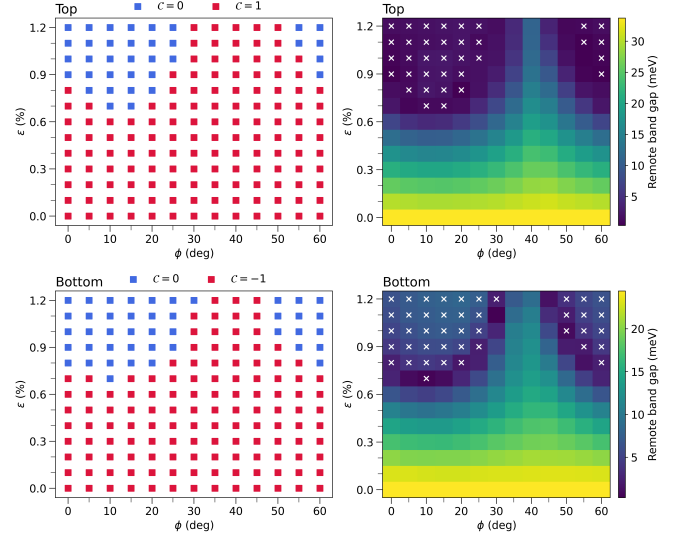


FIG. 11. Strain-induced topology evolution of the top and bottom narrow bands with electrostatic interaction (self-consistent Hartree potential), at $\theta = 1.05^\circ$ with uniaxial heterostrain, for a filling of $\nu = +2$ electrons per moiré unit cell and dielectric constant $\epsilon_r = 7$. The top (bottom) panel shows the Chern number in the top (bottom) narrow band, and their corresponding gap to the remote bands, as a function of the uniaxial strain direction ϕ and magnitude ϵ ; the white crosses in the remote band gap indicate where the narrow band is trivial ($C = 0$). Due to the electrostatic interactions, the topological transitions $|C| = 1 \rightarrow 0$ at which the remote band gap closes and the reopens is different for each narrow band, leading to strain configuration at which only one band topological (or trivial).

Perturbation	Topology Change	References
Strain	✓	[77, 102], This work
Hartree	✗	[59, 60]
Substrate	✓	[100]
Displacement field	✗	[107, 108]

TABLE I. Possible perturbations and their effect on being able to change the topology of the narrow bands in twisted bilayer graphene. The four perturbations are assumed to act on TBG at a fixed twist angle (e.g, the magic angle $\theta = 1.05^\circ$), with a small mass term $\sim \sigma_z m$ that opens a gap at the Dirac points. The topological nature of the bands is taken with respect to transitions between nonzero and zero valley Chern numbers in the top and bottom narrow bands. The Hartree potential is assumed to be for fillings between $-4 \leq \nu \leq 4$. Non-listed perturbations involving two or more effects (e.g., strain and electrostatic interactions) can always change the topology of the narrow bands.

of the perturbations act in conjunction, the topology can always change (e.g., strain with Hartree, or Hartree with displacement field, and so on).

Topology changes in the narrow bands, by means of any of the listed perturbations in Table I, pose a restric-

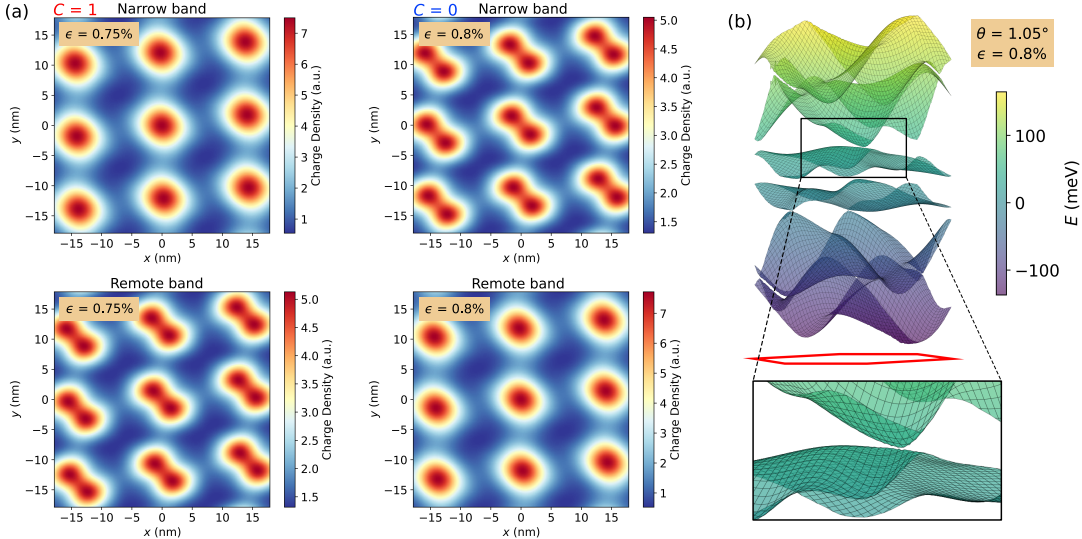


FIG. 12. (a) Charge density $\rho_{\mathbf{k}}(\mathbf{r})$ in the top narrow band and the closest remote band, at the momentum point \mathbf{k} of minimum direct gap between them, for twist angle $\theta = 1.05^\circ$ and uniaxial strain at $\phi = 20^\circ$, with magnitudes $\epsilon = 0.75\%$ and $\epsilon = 0.8\%$. The transition from a topological ($C = 1$) to trivial ($C = 0$) narrow band takes place between the two strain magnitudes (cf. Figure 10). When the transition occurs there is a charge density transfer from the top to the remote band. Panel (b) shows the noninteracting 3D band structure for the uniaxial strain magnitude $\epsilon = 0.8\%$. The zoom inset highlights the minimum gap between the top narrow band and the remote band, at which the charge transfer takes place.

tion on topological heavy fermion models of the narrow bands in TSBG [49, 109, 110], as they rely on the topological nature of the bands.

VI. CONCLUSION

In summary, we studied the combined effects of twist and strain in bilayer graphene using atomistic tight-binding and strain-extended continuum models. Strain reshapes the moiré geometry, broadens the narrow bands, splits the vHs, lifts valley degeneracy, and shifts the Dirac points within the mBZ. The shear strain introduces stronger distortion of both the geometrical and electronic properties. Moreover, the strain direction is crucial: it controls both the bandwidth and the valley-resolved topology, and shifts the twist angle that minimizes the bandwidth. A continuum model with strain-induced scalar and gauge fields reproduces the atomistic spectra and the strain-driven topological transitions that occur when the gap to the remote bands closes and re-opens. Including electrostatic (Hartree) interactions, we find nonrigid spectral shifts at low strain that evolve toward an almost rigid shift at higher strain; the interaction mainly reshapes the bands without reversing the strain-induced broadening. Finally, we develop a general method based on the energy minimization, to determine the twist and strain from the STM topography. These results show that strain provides a practical knob to control band structure and valley topology in moiré graphene.

ACKNOWLEDGMENTS

We thank Mikito Koshino and Eduardo V. Castro for fruitful discussions. Z.Z. thanks Wei Li for the discussion in the 2DSPM conference in San Sebastián, which inspired the initial idea of this work. IMDEA Nanociencia acknowledges support from the “Severo Ochoa” Programme for Centres of Excellence in R&D (Grant No. SEV-2016-0686), and from NOVMOMAT, Grant PID2022-142162NB-I00 funded by MCIN/AEI/10.13039/501100011033 and, by “ERDF A way of making Europe”. F.E. acknowledges support funding from the European Union’s Horizon 2020 research and innovation programme under the Marie Skłodowska-Curie grant agreement No 101210351. Z.Z. acknowledges support funding from the European Union’s Horizon 2020 research and innovation programme under the Marie Skłodowska-Curie grant agreement No 101034431 and from the “Severo Ochoa” Programme for Centres of Excellence in R&D (CEX2020-001039-S / AEI / 10.13039/501100011033). P.A.P acknowledges funding by Grant No. JSF-24-05-0002 of the Julian Schwinger Foundation for Physics Research. S.Y. acknowledges funding from the National Natural Science Foundation of China (Grants No. 12425407, 12174291), the Natural Science Foundation of Hubei Province, China (Grant No. 2023BAA020). Numerical calculations presented in this paper have been performed in the Supercomputing Center of Wuhan University.

DATA AVAILABILITY

All data needed to evaluate the conclusions in the paper are present in the paper and/or the Supplementary Materials.

CODE AVAILABILITY

The codes that support the findings of this study are available from the corresponding authors on reasonable request.

AUTHOR CONTRIBUTIONS

ZZ and FE supervised the project. DW performed the tight-binding calculations with the help of ZZ. FE performed the continuum calculations. All authors discussed the results. FE, DW and ZZ co-wrote the manuscript with inputs from all the authors.

COMPETING INTERESTS

The authors declare no competing interests.

[1] E. Y. Andrei, D. K. Efetov, P. Jarillo-Herrero, A. H. MacDonald, K. F. Mak, T. Senthil, E. Tutuc, A. Yazdani, and A. F. Young, The marvels of moiré materials, *Nature Reviews Materials* **6**, 201–206 (2021).

[2] Y. Cao, V. Fatemi, A. Demir, S. Fang, S. L. Tomarken, J. Y. Luo, J. D. Sanchez-Yamagishi, K. Watanabe, T. Taniguchi, E. Kaxiras, R. C. Ashoori, and P. Jarillo-Herrero, Correlated insulator behaviour at half-filling in magic-angle graphene superlattices, *Nature* **556**, 80 (2018).

[3] Y. Cao, V. Fatemi, S. Fang, K. Watanabe, T. Taniguchi, E. Kaxiras, and P. Jarillo-Herrero, Unconventional superconductivity in magic-angle graphene superlattices, *Nature* **556**, 43 (2018).

[4] A. Kervelsky, L. J. McGilly, D. M. Kennes, L. Xian, M. Yankowitz, S. Chen, K. Watanabe, T. Taniguchi, J. Hone, C. Dean, A. Rubio, and A. N. Pasupathy, Maximized electron interactions at the magic angle in twisted bilayer graphene, *Nature* **572**, 95 (2019).

[5] M. Yankowitz, S. Chen, H. Polshyn, Y. Zhang, K. Watanabe, T. Taniguchi, D. Graf, A. F. Young, and C. R. Dean, Tuning superconductivity in twisted bilayer graphene, *Science* **363**, 1059 (2019).

[6] X. Lu, P. Stepanov, W. Yang, M. Xie, M. A. Aamir, I. Das, C. Urgell, K. Watanabe, T. Taniguchi, G. Zhang, *et al.*, Superconductors, orbital magnets and correlated states in magic-angle bilayer graphene, *Nature* **574**, 653 (2019).

[7] Y. Saito, J. Ge, K. Watanabe, T. Taniguchi, and A. F. Young, Independent superconductors and correlated insulators in twisted bilayer graphene, *Nature Physics* **16**, 926 (2020).

[8] U. Zondiner, A. Rozen, D. Rodan-Legrain, Y. Cao, R. Queiroz, T. Taniguchi, K. Watanabe, Y. Oreg, F. von Oppen, A. Stern, *et al.*, Cascade of phase transitions and dirac revivals in magic-angle graphene, *Nature* **582**, 203 (2020).

[9] Y. Xu, S. Liu, D. A. Rhodes, K. Watanabe, T. Taniguchi, J. Hone, V. Elser, K. F. Mak, and J. Shan, Correlated insulating states at fractional fillings of moiré superlattices, *Nature* **587**, 214 (2020).

[10] Y. Choi, H. Kim, Y. Peng, A. Thomson, C. Lewandowski, R. Polski, Y. Zhang, H. S. Arora, K. Watanabe, T. Taniguchi, *et al.*, Correlation-driven topological phases in magic-angle twisted bilayer graphene, *Nature* **589**, 536 (2021).

[11] Y. Cao, D. Rodan-Legrain, J. M. Park, N. F. Yuan, K. Watanabe, T. Taniguchi, R. M. Fernandes, L. Fu, and P. Jarillo-Herrero, Nematicity and competing orders in superconducting magic-angle graphene, *Science* **372**, 264 (2021).

[12] J. Lopes dos Santos, N. Peres, and A. Castro Neto, Graphene bilayer with a twist: Electronic structure, *Physical Review Letters* **99**, 256802 (2007).

[13] G. Trambly de Laissardière, D. Mayou, and L. Magaud, Localization of dirac electrons in rotated graphene bilayers, *Nano letters* **10**, 804 (2010).

[14] E. Suárez Morell, J. Correa, P. Vargas, M. Pacheco, and Z. Barticevic, Flat bands in slightly twisted bilayer graphene: Tight-binding calculations, *Physical Review B* **82**, 121407 (2010).

[15] R. Bistritzer and A. H. MacDonald, Moiré bands in twisted double-layer graphene, *Proceedings of the National Academy of Sciences* **108**, 12233 (2011).

[16] E. Y. Andrei and A. H. MacDonald, Graphene bilayers with a twist, *Nature Materials* **19**, 1265–1275 (2020).

[17] P. Moon and M. Koshino, Optical absorption in twisted bilayer graphene, *Physical Review B* **87**, 205404 (2013).

[18] M. Koshino, Interlayer interaction in general incommensurate atomic layers, *New Journal of Physics* **17**, 015014 (2015).

[19] P. San-Jose, J. González, and F. Guinea, Non-abelian gauge potentials in graphene bilayers, *Physical Review Letters* **108**, 10.1103/physrevlett.108.216802 (2012).

[20] Z. Bi, N. F. Q. Yuan, and L. Fu, Designing flat bands by strain, *Physical Review B* **100**, 035448 (2019).

[21] F. Escudero, A. Simmer, Z. Zhan, P. A. Pantaleón, and F. Guinea, Designing moiré patterns by strain, *Physical Review Research* **6**, 023203 (2024).

[22] G. Tarnopolsky, A. J. Kruchkov, and A. Vishwanath, Origin of magic angles in twisted bilayer graphene, *Physical Review Letters* **122**, 106405 (2019).

[23] M. Kapfer, B. S. Jessen, M. E. Eisele, M. Fu, D. R. Danielsen, T. P. Darlington, S. L. Moore, N. R. Finney, A. Marchese, V. Hsieh, *et al.*, Programming twist angle and strain profiles in 2d materials, *Science* **381**, 677 (2023).

[24] Y. Hou, J. Zhou, M. Xue, M. Yu, Y. Han, Z. Zhang, and Y. Lu, Strain engineering of twisted bilayer graphene: The rise of strain-twistrionics, *Small* **21**, 2311185 (2024).

[25] J. S. Alden, A. W. Tsen, P. Y. Huang, R. Hovden, L. Brown, J. Park, D. A. Muller, and P. L. McEuen, Strain solitons and topological defects in bilayer graphene, *Proceedings of the National Academy of Sciences* **110**, 11256 (2013).

[26] C.-C. Lu, Y.-C. Lin, Z. Liu, C.-H. Yeh, K. Suenaga, and P.-W. Chiu, Twisting bilayer graphene superlattices, *ACS Nano* **7**, 2587 (2013).

[27] S. W. Schmucker, C. D. Cress, J. C. Culbertson, J. W. Beeman, O. D. Dubon, and J. T. Robinson, Raman sig-

nature of defected twisted bilayer graphene, *Carbon* **93**, 250 (2015).

[28] J. H. Wilson, Y. Fu, S. Das Sarma, and J. Pixley, Disorder in twisted bilayer graphene, *Physical Review Research* **2**, 023325 (2020).

[29] A. Schäpers, J. Sonntag, L. Valerius, B. Pestka, J. Strasdas, K. Watanabe, T. Taniguchi, L. Wirtz, M. Morgenstern, B. Beschoten, *et al.*, Raman imaging of twist angle variations in twisted bilayer graphene at intermediate angles, *2D Materials* **9**, 045009 (2022).

[30] T. E. Beechem, T. Ohta, B. Diaconescu, and J. T. Robinson, Rotational disorder in twisted bilayer graphene, *ACS Nano* **8**, 1655 (2014).

[31] A. C. Gadelha, D. A. Ohlberg, F. C. Santana, G. S. Eliel, J. S. Lemos, V. Ornelas, D. Miranda, R. B. Nadas, K. Watanabe, T. Taniguchi, *et al.*, Twisted bilayer graphene: a versatile fabrication method and the detection of variable nanometric strain caused by twist-angle disorder, *ACS Applied Nano Materials* **4**, 1858 (2021).

[32] L. Huder, A. Artaud, T. Le Quang, G. T. De Laisserdière, A. G. Jansen, G. Lapertot, C. Chapelier, and V. T. Renard, Electronic spectrum of twisted graphene layers under heterostrain, *Physical Review Letters* **120**, 156405 (2018).

[33] N. P. Kazmierczak, M. Van Winkle, C. Ophus, K. C. Bustillo, S. Carr, H. G. Brown, J. Ciston, T. Taniguchi, K. Watanabe, and D. K. Bediako, Strain fields in twisted bilayer graphene, *Nature Materials* **20**, 956 (2021).

[34] F. Mesple, A. Missaoui, T. Cea, L. Huder, F. Guinea, G. Trambly de Laissardière, C. Chapelier, and V. T. Renard, Heterostrain determines flat bands in magic-angle twisted graphene layers, *Physical Review Letters* **127**, 126405 (2021).

[35] M. Mannaï and S. Haddad, Twistrionics versus straintronics in twisted bilayers of graphene and transition metal dichalcogenides, *Physical Review B* **103**, L201112 (2021).

[36] A. Sinner, P. A. Pantaleón, and F. Guinea, Strain-Induced Quasi-1D Channels in Twisted Moiré Lattices, *Physical Review Letters* **131**, 166402 (2023).

[37] X. Wang, J. Finney, A. L. Sharpe, L. K. Rodenbach, C. L. Hsueh, K. Watanabe, T. Taniguchi, M. Kastner, O. Vafek, and D. Goldhaber-Gordon, Unusual magnetotransport in twisted bilayer graphene from strain-induced open fermi surfaces, *Proceedings of the National Academy of Sciences* **120**, e2307151120 (2023).

[38] Y. Jiang, J. Mao, J. Duan, X. Lai, K. Watanabe, T. Taniguchi, and E. Y. Andrei, Visualizing strain-induced pseudomagnetic fields in graphene through an hbn magnifying glass, *Nano Letters* **17**, 2839–2843 (2017).

[39] J. Mao, S. P. Milovanović, M. Andelković, X. Lai, Y. Cao, K. Watanabe, T. Taniguchi, L. Covaci, F. M. Peeters, A. K. Geim, Y. Jiang, and E. Y. Andrei, Evidence of flat bands and correlated states in buckled graphene superlattices, *Nature* **584**, 215–220 (2020).

[40] T. Peña, A. Dey, S. A. Chowdhury, A. Azizimanesh, W. Hou, A. Sewaket, C. Watson, H. Askari, and S. M. Wu, Moiré engineering in 2d heterostructures with process-induced strain, *Applied Physics Letters* **122**, 143101 (2023).

[41] M. Kögl, P. Soubelet, M. Brotons-Gisbert, A. V. Stier, B. D. Gerardot, and J. J. Finley, Moiré straintronics: a universal platform for reconfigurable quantum materials, *npj 2D Materials and Applications* **7**, 32 (2023).

[42] N. Hasan, T. Peña, A. Dey, D. Yoon, Z. Islam, Y. Zhang, M. V. G. Leal, A. M. van der Zande, H. Askari, and S. M. Wu, Strain-induced moiré reconstruction and memorization in two-dimensional materials without twist, *arXiv* **10.48550/ARXIV.2510.13699** (2025).

[43] X. Gao, H. Sun, D.-H. Kang, C. Wang, Q. J. Wang, and D. Nam, Heterostrain-enabled dynamically tunable moiré superlattice in twisted bilayer graphene, *Scientific Reports* **11**, 21402 (2021).

[44] I. Sequeira, A. Z. Barabas, A. H. Barajas-Aguilar, M. G. Bacani, N. Nakatsuji, M. Koshino, T. Taniguchi, K. Watanabe, and J. D. Sanchez-Yamagishi, Manipulating moires by controlling heterostrain in van der waals devices, *Nano Letters* **24**, 15662 (2024).

[45] Y. Xie, B. Lian, B. Jäck, X. Liu, C.-L. Chiu, K. Watanabe, T. Taniguchi, B. A. Bernevig, and A. Yazdani, Spectroscopic signatures of many-body correlations in magic-angle twisted bilayer graphene, *Nature* **572**, 101 (2019).

[46] J. Yu, G. Jia, Q. Li, Z. Zhan, Y. Wang, K. Xiao, Y. Ju, H. Zhang, Z. Hu, Y. Guo, B. Lian, P. Tang, P. A. Pantaleón, S. Zhou, F. Guinea, Q.-K. Xue, and W. Li, Twist angle driven electronic structure evolution of twisted bilayer graphene, *arxiv* **10.48550/ARXIV.2406.20040** (2025).

[47] P. Ouyang, J. Yu, Q. Li, G. Jia, Y. Wang, K. Xiao, H. Zhang, Z. Hu, P. A. Pantaleón, Z. Zhan, S. Zhou, F. Guinea, Q.-K. Xue, and W. Li, Structural and electronic signatures of strain-tunable marginally twisted bilayer graphene, *National Science Review* **10.1093/nsr/nwaf568** (2025).

[48] R. Carrasco, F. Escudero, Z. Zhan, E. C.-d. Rio, B. Viña-Bausa, Y. Maximenko, P. A. Pantaleón, F. Guinea, and I. Brihuega, Twistraintronics in square moire superlattices of stacked graphene layers, *arXiv* **10.48550/ARXIV.2511.04741** (2025).

[49] J. Herzog-Arbeitman, J. Yu, D. Calugaru, H. Hu, N. Regnault, O. Vafek, J. Kang, and B. A. Bernevig, Topological heavy fermion model as an efficient representation of atomistic strain and relaxation in twisted bilayer graphene, *Physical Review B* **112**, 10.1103/xv3m-vtlr (2025).

[50] J. Herzog-Arbeitman, D. Călugăru, H. Hu, J. Yu, N. Regnault, J. Kang, B. A. Bernevig, and O. Vafek, Kekulé spiral order from strained topological heavy fermions, *Physical Review B* **112**, 10.1103/rr5g-3js8 (2025).

[51] A. Zhu, D. Bennett, D. T. Larson, M. M. A. Ezzi, E. Manousakis, and E. Kaxiras, Twisted bilayer graphene from first-principles: structural and electronic properties, *arXiv* **10.48550/ARXIV.2601.16851** (2026).

[52] M. Gonçalves, B. Amorim, F. Riche, E. V. Castro, and P. Ribeiro, Incommensurability enabled quasi-fractal order in 1d narrow-band moiré systems, *Nature Physics* **20**, 1933–1940 (2024).

[53] V. M. Pereira, A. Castro Neto, and N. Peres, Tight-binding approach to uniaxial strain in graphene, *Physical Review B* **80**, 045401 (2009).

[54] M. A. Vozmediano, M. Katsnelson, and F. Guinea, Gauge fields in graphene, *Physics Reports* **496**, 109 (2010).

[55] B. Amorim, A. Cortijo, F. De Juan, A. G. Grushin,

F. Guinea, A. Gutiérrez-Rubio, H. Ochoa, V. Parente, R. Roldán, P. San-Jose, *et al.*, Novel effects of strains in graphene and other two dimensional materials, *Physics Reports* **617**, 1 (2016).

[56] G. G. Naumis, S. Barraza-Lopez, M. Oliva-Leyva, and H. Terrones, Electronic and optical properties of strained graphene and other strained 2d materials: a review, *Reports on Progress in Physics* **80**, 096501 (2017).

[57] H. Suzuura and T. Ando, Phonons and electron-phonon scattering in carbon nanotubes, *Physical review B* **65**, 235412 (2002).

[58] J. L. Manes, Symmetry-based approach to electron-phonon interactions in graphene, *Physical Review B* **76**, 045430 (2007).

[59] F. Guinea and N. R. Walet, Electrostatic effects, band distortions, and superconductivity in twisted graphene bilayers, *Proceedings of the National Academy of Sciences* **115**, 13174 (2018).

[60] T. Cea, N. R. Walet, and F. Guinea, Electronic band structure and pinning of fermi energy to van hove singularities in twisted bilayer graphene: A self-consistent approach, *Physical Review B* **100**, 205113 (2019).

[61] Z. A. Goodwin, V. Vitale, X. Liang, A. A. Mostofi, and J. Lischner, Hartree theory calculations of quasiparticle properties in twisted bilayer graphene, *Electronic Structure* **2**, 034001 (2020).

[62] T. Cea and F. Guinea, Coulomb interaction, phonons, and superconductivity in twisted bilayer graphene, *Proceedings of the National Academy of Sciences* **118**, e2107874118 (2021).

[63] V. T. Phong, P. A. Pantaleón, T. Cea, and F. Guinea, Band structure and superconductivity in twisted trilayer graphene, *Physical Review B* **104**, L121116 (2021).

[64] D. E. Parker, T. Soejima, J. Hauschild, M. P. Zaletel, and N. Bultinck, Strain-induced quantum phase transitions in magic-angle graphene, *Physical Review Letters* **127**, 027601 (2021).

[65] G. Wagner, Y. H. Kwan, N. Bultinck, S. H. Simon, and S. Parameswaran, Global phase diagram of the normal state of twisted bilayer graphene, *Physical Review Letters* **128**, 156401 (2022).

[66] H. Hu, G. Rai, L. Crippa, J. Herzog-Arbeitman, D. Călugăru, T. Wehling, G. Sangiovanni, R. Valentí, A. M. Tsvelik, and B. A. Bernevig, Symmetric kondo lattice states in doped strained twisted bilayer graphene, *Physical Review Letters* **131**, 166501 (2023).

[67] E. J. Mele, Commensuration and interlayer coherence in twisted bilayer graphene, *Physical Review B* **81**, 161405 (2010).

[68] G. Trambly de Laissardière, D. Mayou, and L. Magaud, Numerical studies of confined states in rotated bilayers of graphene, *Physical Review B* **86**, 125413 (2012).

[69] L. D. Landau, L. Pitaevskii, A. M. Kosevich, and E. M. Lifshitz, *Theory of elasticity: volume 7*, Vol. 7 (Elsevier, 2012).

[70] M. E. Gurtin, E. Fried, and L. Anand, *The mechanics and thermodynamics of continua* (Cambridge university press, 2010).

[71] F. Escudero, Z. Zhan, P. A. Pantaleón, and F. Guinea, Moiré-driven equilibrium, arXiv 10.48550/ARXIV.2601.00948 (2026).

[72] A. Artaud, L. Magaud, T. Le Quang, V. Guisset, P. David, C. Chapelier, and J. Coraux, Universal classification of twisted, strained and sheared graphene moiré superlattices, *Scientific Reports* **6**, 25670 (2016).

[73] X. Lai, G. Li, A. M. Coe, J. H. Pixley, K. Watanabe, T. Taniguchi, and E. Y. Andrei, Moiré periodic and quasiperiodic crystals in heterostructures of twisted bilayer graphene on hexagonal boron nitride, *Nature materials* **1** (2025).

[74] A. Ramires and J. L. Lado, Electrically Tunable Gauge Fields in Tiny-Angle Twisted Bilayer Graphene, *Physical Review Letters* **121**, 146801 (2018).

[75] A. Ramires and J. L. Lado, Impurity-induced triple point fermions in twisted bilayer graphene, *Physical Review B* **99**, 245118 (2019).

[76] S. Plimpton, Fast parallel algorithms for short-range molecular dynamics, *Journal of Computational Physics* **117**, 1–19 (1995).

[77] P. A. Pantaleón, V. T. Phong, G. G. Naumis, and F. Guinea, Interaction-enhanced topological hall effects in strained twisted bilayer graphene, *Physical Review B* **106**, L161101 (2022).

[78] M. Oliva-Leyva and G. G. Naumis, Understanding electron behavior in strained graphene as a reciprocal space distortion, *Physical Review B* **88**, 085430 (2013).

[79] M. Oliva-Leyva and G. G. Naumis, Generalizing the fermi velocity of strained graphene from uniform to nonuniform strain, *Physics Letters A* **379**, 2645–2651 (2015).

[80] M. Koshino, N. F. Yuan, T. Koretsune, M. Ochi, K. Kuroki, and L. Fu, Maximally localized wannier orbitals and the extended hubbard model for twisted bilayer graphene, *Physical Review X* **8**, 031087 (2018).

[81] M. Koshino and N. N. T. Nam, Effective continuum model for relaxed twisted bilayer graphene and moiré electron-phonon interaction, *Physical Review B* **101**, 10.1103/physrevb.101.195425 (2020).

[82] S. Carr, S. Fang, Z. Zhu, and E. Kaxiras, Exact continuum model for low-energy electronic states of twisted bilayer graphene, *Physical Review Research* **1**, 10.1103/physrevresearch.1.013001 (2019).

[83] V. H. Nguyen and P. Dollfus, Strain-induced modulation of dirac cones and van hove singularities in a twisted graphene bilayer, *2D Materials* **2**, 035005 (2015).

[84] M. Long, Z. Zhan, P. A. Pantaleón, J. A. Silva-Guillén, F. Guinea, and S. Yuan, Electronic properties of twisted bilayer graphene suspended and encapsulated with hexagonal boron nitride, *Physical Review B* **107**, 115140 (2023).

[85] M. Long, P. A. Pantaleón, Z. Zhan, F. Guinea, J. A. Silva-Guillén, and S. Yuan, An atomistic approach for the structural and electronic properties of twisted bilayer graphene-boron nitride heterostructures, *npj Computational Materials* **8**, 73 (2022).

[86] G. Li, R. Krishna Kumar, P. Stepanov, P. A. Pantaleón, Z. Zhan, H. Agarwal, A. Bercher, J. Barrier, K. Watanabe, T. Taniguchi, A. B. Kuzmenko, F. Guinea, I. Torre, and F. H. L. Koppens, Infrared spectroscopy for diagnosing superlattice minibands in twisted bilayer graphene near the magic angle, *Nano Letters* **24**, 15956–15963 (2024).

[87] F. Escudero, Diagrammatic perturbation approach to moiré bands in twisted bilayer graphene, *Physical Review B* **110**, 045442 (2024).

[88] S.-M. Choi, S.-H. Jhi, and Y.-W. Son, Controlling energy gap of bilayer graphene by strain, *Nano Letters* **10**, 3486 (2010).

[89] F. Guinea and N. R. Walet, Continuum models for twisted bilayer graphene: Effect of lattice deformation and hopping parameters, *Physical Review B* **99**, 205134 (2019).

[90] I. V. Lebedeva and A. M. Popov, Two phases with different domain wall networks and a reentrant phase transition in bilayer graphene under strain, *Physical Review Letters* **124**, 116101 (2020).

[91] F. Mesple, N. R. Walet, G. Trambly de Laissardi  re, F. Guinea, D. Do  enovi  , H. Okuno, C. Paillet, A. Michon, C. Chapelier, and V. T. Renard, Giant atomic swirl in graphene bilayers with biaxial heterostrain, *Advanced Materials* **35**, e2306312 (2023).

[92] V. Hung Nguyen, D. Paszko, M. Lamparski, B. Van Troeye, V. Meunier, and J.-C. Charlier, Electronic localization in small-angle twisted bilayer graphene, *2D Materials* **8**, 035046 (2021).

[93] A. Timmel and E. Mele, Dirac-harper theory for one-dimensional moir   superlattices, *Physical Review Letters* **125**, 166803 (2020).

[94] J. Kang and O. Vafek, Analytical solution for the relaxed atomic configuration of twisted bilayer graphene including heterostrain, *Physical Review B* **112**, 125138 (2025).

[95] S. Fang, S. Carr, Z. Zhu, D. Massatt, and E. Kaxiras, Angle-dependent *ab initio* low-energy hamiltonians for a relaxed twisted bilayer graphene heterostructure, arxiv [10.48550/ARXIV.1908.00058](https://arxiv.org/abs/10.48550/ARXIV.1908.00058) (2019).

[96] V. Hsieh, D. Halbertal, N. R. Finney, Z. Zhu, E. Gerber, M. Pizzochero, E. Kucukbenli, G. R. Schleider, M. Angheli, K. Watanabe, *et al.*, Domain-dependent surface adhesion in twisted few-layer graphene: Platform for moir  -assisted chemistry, *Nano Letters* **23**, 3137 (2023).

[97] P. Cazeaux, D. Clark, R. Engelke, P. Kim, and M. Luskin, Relaxation and domain wall structure of bilayer moir   systems, *Journal of Elasticity* **154**, 443 (2023).

[98] B. A. Bernevig, Z.-D. Song, N. Regnault, and B. Lian, Twisted bilayer graphene. iii. interacting hamiltonian and exact symmetries, *Physical Review B* **103**, 205413 (2021).

[99] L. Rademaker and P. Mellado, Charge-transfer insulation in twisted bilayer graphene, *Physical Review B* **98**, 235158 (2018).

[100] T. Cea and F. Guinea, Band structure and insulating states driven by coulomb interaction in twisted bilayer graphene, *Physical Review B* **102**, 045107 (2020).

[101] M. M. A. Ezzi, L. Peng, Z. Liu, J. H. Z. Chao, G. N. Pallewela, D. Foo, and S. Adam, A self-consistent hartree theory for lattice-relaxed magic-angle twisted bilayer graphene, arXiv [10.48550/ARXIV.2404.17638](https://arxiv.org/abs/10.48550/ARXIV.2404.17638) (2024).

[102] P. A. Pantale  n, T. Low, and F. Guinea, Tunable large berry dipole in strained twisted bilayer graphene, *Physical Review B* **103**, 205403 (2021).

[103] I. Sodemann and L. Fu, Quantum nonlinear hall effect induced by berry curvature dipole in time-reversal invariant materials, *Physical Review Letters* **115**, 216806 (2015).

[104] T. Low, Y. Jiang, and F. Guinea, Topological currents in black phosphorus with broken inversion symmetry, *Physical Review B* **92**, 235447 (2015).

[105] S. Sinha, P. C. Adak, A. Chakraborty, K. Das, K. Debnath, L. D. V. Sangani, K. Watanabe, T. Taniguchi, U. V. Waghmare, A. Agarwal, and M. M. Deshmukh, Berry curvature dipole senses topological transition in a moir   superlattice, *Nature Physics* **18**, 765–770 (2022).

[106] T. Fukui, Y. Hatsugai, and H. Suzuki, Chern numbers in discretized brillouin zone: Efficient method of computing (spin) hall conductances, *Journal of the Physical Society of Japan* **74**, 1674 (2005).

[107] X. Gao, A. Jimeno-Pozo, P. A. Pantaleon, E. Codecido, D. L. Sharifi, Z. Zhang, Y. Liu, K. Watanabe, T. Taniguchi, M. W. Bockrath, F. Guinea, and C. N. Lau, Double-edged role of interactions in superconducting twisted bilayer graphene, arXiv [10.48550/ARXIV.2412.01578](https://arxiv.org/abs/10.48550/ARXIV.2412.01578) (2024).

[108] R. Dutta, A. Ghosh, S. Mandal, K. Watanabe, T. Taniguchi, H. Krishnamurthy, S. Banerjee, M. Jain, and A. Das, Electric field-tunable superconductivity with competing orders in twisted bilayer graphene near the magic angle, *ACS Nano* **19**, 5353 (2025).

[109] Z.-D. Song and B. A. Bernevig, Magic-angle twisted bilayer graphene as a topological heavy fermion problem, *Physical Review Letters* **129**, 047601 (2022).

[110] H. Shi and X. Dai, Heavy-fermion representation for twisted bilayer graphene systems, *Physical Review B* **106**, 245129 (2022).